Sedimentary architecture, depositional facies and diagenetic response to intracratonic deformation and climate change inferred from outcrops for a pivotal period (Jurassic/Cretaceous boundary, Paris Basin, France)

Benjamin Brigaud [a,*], Benoît Vincent [b], Maurice Pagel [a], Antoine Gras [a], Aurélie Noret [a], Philippe Landrein [c], Emilia Huret [d]

[a] GEOPS, Univ. Paris-Sud, CNRS, Université Paris-Saclay, 91405 Orsay, France
[b] Cambridge Carbonate Ltd., 1 rue de Varoux, 21120 Marey-sur-Tille, France
[c] Andra, Route Départementale 960, 55290 Bure, France
[d] Andra, 1-7 rue Jean Monnet, 92298 Châtenay-Malabry Cedex, France

ARTICLE INFO

ABSTRACT

The aim of this study is to decipher the respective influences of geodynamic and climate disturbances at the Jurassic/Cretaceous boundary on sedimentary facies and carbonate diagenesis in a stable intracratonic basin using isotopic geochemistry and subsidence quantification. Fourteen lithofacies were deposited in a (1) carbonate platform and (2) a delta plain environment. Climate change from cool and wet to warm and semi-arid conditions during the early Tithonian influenced the syn-sedimentary dolomitization process within the carbonate platform during the mid-Tithonian. Architecture and facies reconstructions well-constrained the Jurassic-Cretaceous Unconformity (JCU), which was an important local structural episode marked by (1) an 80 m uplift in the eastern Paris Basin and by (2) the formation of a NW–SE low wavelength 15 km-wide and 30 km-long flexure. This first tectonic event tended to maintain brine ponds and supratidal marsh environments in the platform during the late Tithonian and early Berriasian, forming Purbeckian facies and associated dolomitic facies. A major depositional change occurred between the early and late Berriasian from shallow carbonate platform environments to fluviatile-deltaic clastic deposits (Wealden facies). This facies change is underlain by a major unconformity corresponding to the Ryazanian unconformity. It is marked (1) by erosion processes, karstification of the carbonate substrate, and the development of ferruginous weathering products (goethite), followed by (2) incision processes in a fluvial-deltaic environment. This unconformity is consecutive to a 40 m uplift in the eastern Paris Basin. The rifting phase in the Bay of Biscay, in the Pyrenee Zone, and in the Artic-North Atlantic together with the opening of the Ligurian Sea had a major influence on the northern part of France by causing uplifts (120 m from the Tithonian) and flexuring. Geodynamics played a major role in carbonate demise in the Paris Basin leading to exposure and karstification of the carbonate platform. Added to the generalized uplift, western Tethyan cool and humid conditions from the late Berriasian caused terrigenous influx into large-scale marine domains which was detrimental and unfavorable to carbonate growth.

1. Introduction

Intracratonic basins are relatively stable areas, characterized by low subsidence rates over long periods (>10 Ma; Guillocheau et al., 2000). Carbonate depositional architectures are therefore commonly controlled by environmental factors such as climate, eustasy, and trophic conditions (Pomar, 2001; Pomar et al., 2017). In these settings, carbonate diagenesis is mostly controlled by increasing pressure and temperature during burial (Pagel et al., 2014). However, several studies of intracratonic basins of the western European domain have shown that

they experienced less stable periods at the origin of deformation and diagenetic events (Hendry, 1993; Jacquin and de Graciansky, 1998b; Guillocheau et al., 2000; Vincent et al., 2007). For instance, the sedimentary record at the Jurassic/Cretaceous boundary is marked by a couple of major unconformities named Late Cimmerian Unconformities (LCU) at the western Tethyan scale, and characterized by generalized uplift and exposure around the London-Brabant, Ardennes, and Armorican massifs, leading to the erosion of Jurassic sediments on the edges of all the surrounding basins (Ziegler, 1988; Sellwood et al., 1989; Hendry, 1993; Rusciadelli, 1996; Jacquin and de Graciansky, 1998a; Guillocheau et al., 2000).

In the Paris Basin, the Late Jurassic to Early Cretaceous sedimentary deposits were then restricted to a NW–SE central area, opening to the

marine domain located beyond the Jura Platform to the east (Mégnien and Mégnien, 1980; Rusciadelli, 1996). This basin allowed the preservation of supratidal argillaceous dolomite, dolomite, and evaporite sediments (Purbeckian facies; Mégnien and Mégnien, 1980, Rusciadelli, 1996) and then sandy fluvial-deltaic sediments (Wealden facies; Allen, 1959; Allen and Wimbledon, 1991; Rusciadelli, 1996). The siliciclastic sources of the Wealden facies were the crystalline rocks of the Armorican and Cornubian Massifs (Allen, 1959). This siliciclastic sedimentation at the beginning of the Cretaceous period contrasts with the thick accumulation of carbonate sediments (about 1300 m) deposited mostly in a shallow-marine platform domain since the beginning of the Jurassic (Brigaud et al., 2014), and that resumed only during the Cenomanian (Mégnien and Mégnien, 1980). Paleoclimate reconstructions carried out over a decade show that important changes also occurred at the Jurassic/Cretaceous boundary (Allen, 1998; Abbink et al., 2001; Schnyder et al., 2009; Dera et al., 2011; Martinez and Dera, 2015; Rogov et al., 2017). During this pivotal period, in contrast to most geological systems, it has been impossible to find geobiological global events, or even regional markers in western Tethyan domain, to made high resolution correlations, which leads some debates with regards to the definition of the Jurassic/Cretaceous boundary (Gradstein et al., 2012). Despite excellent quality outcrops in the eastern Paris Basin, this area has received little attention (Rusciadelli, 1996) compared to other time-equivalent deposits in the Jura, Dorset, and western Paris Basin (Deconinck, 1987; Strasser, 1988; Allen and Wimbledon, 1991; Allen, 1998; Deconinck et al., 2000; Deconinck et al., 2001; Schnyder et al., 2005a, 2009).

The objective of this study is to decipher the respective influences of geodynamics and climate on the sedimentary record in the supposedly stable intracratonic Paris basin, during this critical time period of the Jurassic/Cretaceous transition. Through an integrated facies analysis, depositional environments are interpreted and the stratigraphic architectures reconstructed with the aim of discussing the controls of eustasy and tectonics (subsidence or uplift), as well as climate change, on sedimentation and the possible demise of the Anglo-Parisian Jurassic carbonate platform. A detailed study of the diagenetic processes, with a specific focus on eogenetic phases, that affected the carbonate formations at the Jurassic/Cretaceous boundary is also conducted in order to complete the record of events possibly missing within the unconformities.

From a more applied perspective, it is worth noting that in the eastern part of the Paris basin, the Late Jurassic (Oxfordian and Kimmeridgian/Tithonian) and Early Cretaceous (Berriasian/Valanginian) sedimentary formations studied in this work overlie the Callovian–Oxfordian clay-rich formation where the Andra (French National Agency for Radioactive Waste Management) has built an underground research laboratory to evaluate the feasibility of deep geological storage of radioactive waste. Constraining the sedimentary architectures and characteristics of the rocks deposited at the Jurassic/Cretaceous boundary is thus of critical importance since these formations are supposed to be excavated and engineered during the possible future construction of shafts and access ramps for the underground repository site.

2. Geological setting

The study area is located in the north-eastern part of the Paris Basin where deposits of the Jurassic/Cretaceous boundary crop out (Fig. 1A). Seven sections located in quarries were selected (Fig. 1B): (1) Poissons (Mélaire mines), (2) Magneux, (3) La Fontaine, (4) La Longue Queue, (5) Champ Maillot, (6) Terme, and (7) Givrauval. This dataset is supplemented by previous descriptions of two sections (8) La Couleuvre and (9) La Houpette, (Rusciadelli, 1996) and two boreholes (W1 and W2) from online data (http://infoterre.brgm.fr) of the French Geological Survey (Fig. 1B). The Paris Basin is an intracratonic sedimentary basin which developed above a Cadomian and Variscan basement (Guillocheau et al., 2000). Geodynamic studies of the Paris Basin suggest

that the Mesozoic subsidence is a record of two stacked signals: (1) long-term thermal subsidence and (2) shorter-term ($\times$10 Ma) acceleration-deceleration phases related to Eurasian plate stress variations (Guillocheau, 1991; Jacquin and de Graciansky, 1998b; Guillocheau et al., 2000; Robin et al., 2000). Authors agree that the history of the Paris Basin can be summarized in three main episodes, which in the rock record are separated by major unconformities: (1) a period of high subsidence (Triassic/Jurassic), (2) a period of low subsidence (Early Cretaceous/Eocene) with a brief increased rate during the Late Cretaceous, and (3) a period of uplift (Neogene/Present-day) which modeled the final shape of the present-day Paris Basin (Guillocheau et al., 2000; Robin et al., 2000). This study focuses on a period of drastic geodynamic changes with a pronounced decrease in subsidence at the Jurassic/Cretaceous boundary in the Paris Basin (Guillocheau et al., 2000) and tectonic reorganization affecting the neighboring Southeastern French Basin (Homberg et al., 2013). The facies change from Jurassic shallow marine carbonate platform facies to Early Cretaceous fluvial-estuarine siliciclastics indicates a major regressive event in the Paris Basin, which is also recorded in other European Basins (Jacquin and de Graciansky, 1998a; Guillocheau et al., 2000). During this transition, the London Brabant Massif was uplifted and in the eastern Paris Basin the Jurassic carbonate deposits were eroded and karstified and ferruginous weathering products formed at the top of the Jurassic carbonate platform (Guillocheau et al., 2000; Thiry et al., 2006; Fizaine, 2012). The geodynamic synthesis of the Paris Basin by Guillocheau et al. (2000) described in sediments of the Jurassic/Cretaceous transition the succession of two distinct truncations grouped as the Late Cimmerian Unconformities (LCU; Ziegler, 1990). The first phase corresponds to the Jurassic–Cretaceous Unconformity (JCU), called Base Cretaceous Unconformity (BCU) by Rusciadelli (1996). The terminology JCU is adopted in this study to refer to this first unconformity (JCU = BCU, Guillocheau et al., 2000). The second unconformity corresponds to the Ryazanian Unconformity (RU) of late Berriasian age (Fig. 2; Rusciadelli, 1996; Jacquin and de Graciansky, 1998a; Guillocheau et al., 2000). Late Cimmerian unconformities are recognized in many sedimentary sections from western Europe, North Sea, Norway to East Greenland, commonly at the base of Cretaceous or as intra-Berriasian (Jacquin et al., 1998b; Stoker et al., 2016). In the North Sea, the intra-Berriasian unconformity is generally termed the Late Cimmerian Unconformity (or BCU); (Oakman and Partington, 1998; Stoker et al., 2016). These unconformities are associated with an overall decrease in subsidence in European Basins, an emergence and erosion of large parts of western and central Europe (Jacquin et al., 1998b; Guillocheau et al., 2000; Pharaoh et al., 2010; Stoker et al., 2016). These unconformities are interpreted as the consequence of the stress-induced deflection of the lithosphere, corresponding (1) to the rifting stage in Artic-North Atlantic domain reaching an activity peak during the Jurassic/Cretaceous transition (Mosar et al., 2002; Surlyk, 2003; Stoker et al., 2016) and (2) to the end of rifting in the North Sea (Rawson and Riley, 1982; Lake and Karner, 1987; Ziegler, 1992; Underhill and Partington, 1993; Doré et al., 1999; KyrkjebØ et al., 2004). The decrease of subsidence rate in European Basins and erosion processes of a large part of western Europe leading to this unconformity can also be influenced by Tethyan spreading decreased, by the northeastern movement of the shoulder of the Bay of Biscay rift and by the rifting in the Pyrenean Rift Zone during the Early Cretaceous (Montadert et al., 1979; Ziegler, 1988; Stoker et al., 2016). At the regional plate-scale (NW European Atlantic margin), stress directions change from E-W during the Jurassic with rifting stage in Artic North Atlantic and North Sea to NW-SE during the Early Cretaceous with rifting in Artic North Atlantic only (Doré et al., 1999; Ramail, 2005). At local scale, the associated erosion on the edges of the eastern Paris Basin critically influenced diagenesis of the Jurassic carbonates (Vincent et al., 2007; Brigaud et al., 2009).

Paleogeographic reconstructions show that during the Late Jurassic/Early Cretaceous, the north-eastern Paris Basin was located in tropical to
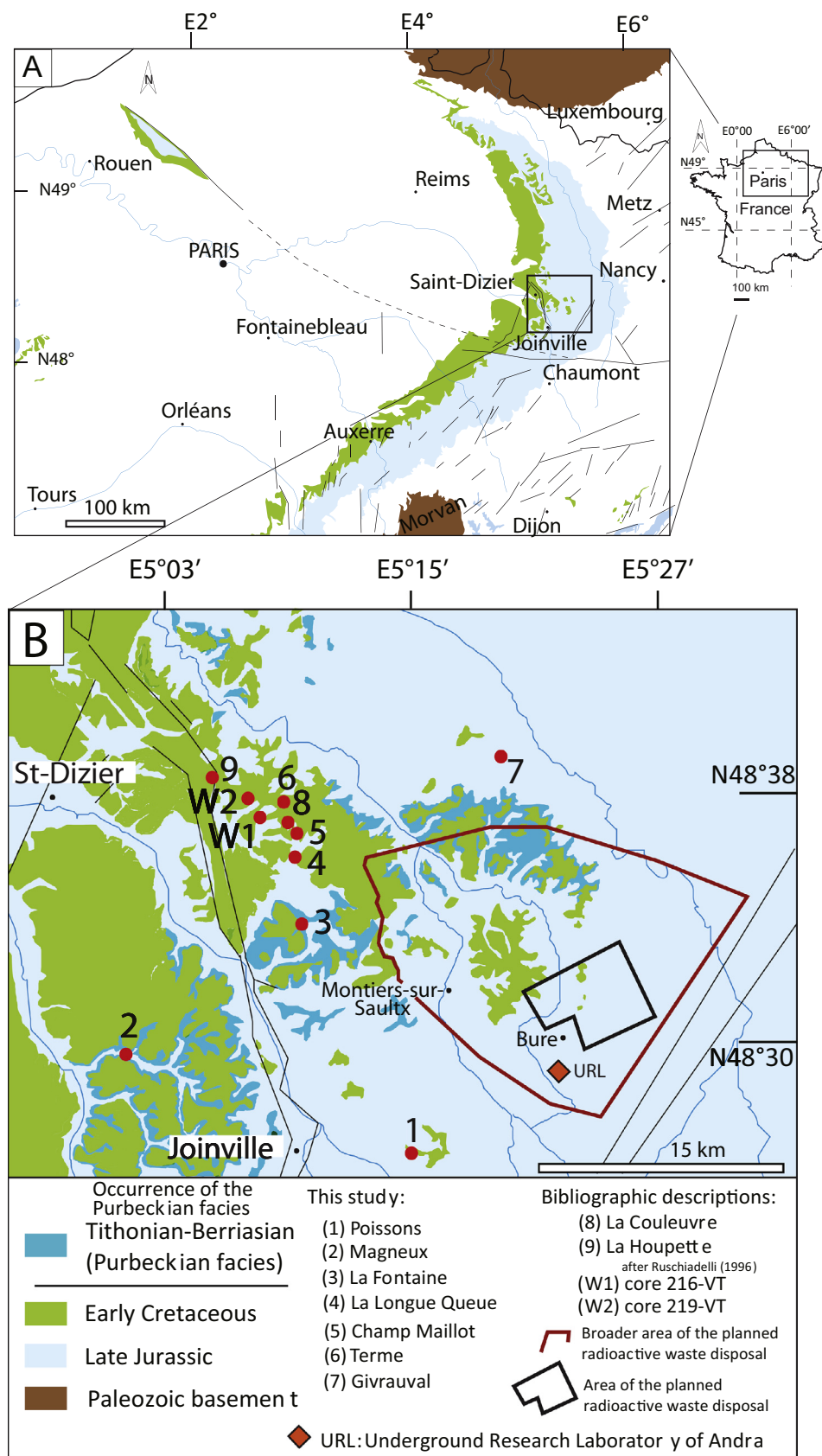
Fig. 1. A- Location of the study area on a geological map of north-eastern France. B- Location of the study outcrops on a simplified geological map of a part of the eastern Paris Basin.
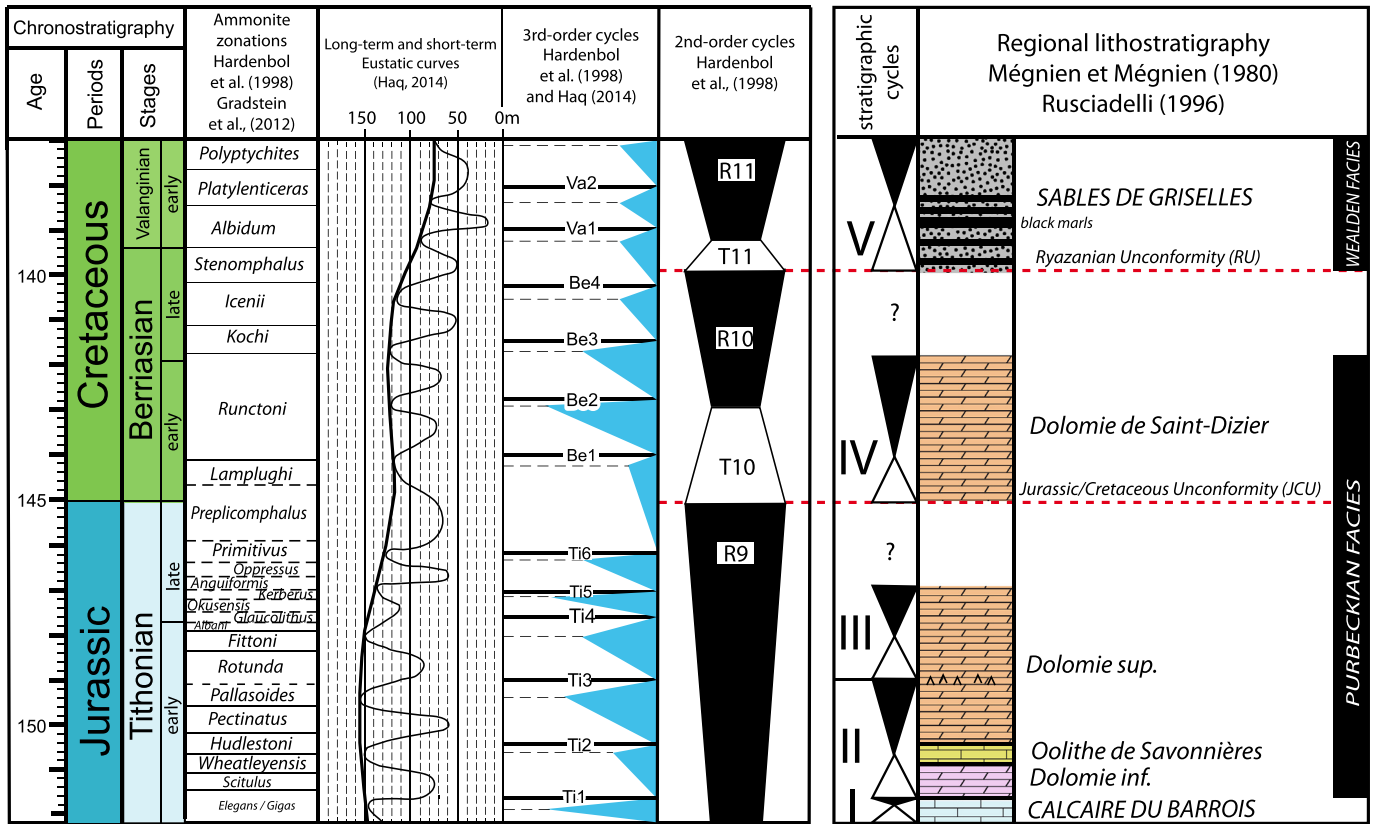
Fig. 2. Schematic regional lithostratigraphic illustration of the study area with ammonite zonations, long-term and short-term eustatic curves, 3rd-order and 2nd-order cycles. Duration of the stages and ammonite zonations from Gradstein et al. (2012). Sea level curves include the long-term envelope and the short-term (third-order) curve (Haq, 2014). Third-order and second-order cycles are numbered following the scheme of Hardenbol et al. (1998).

subtropical latitudes (28–35° N) (Fig. 3, Dercourt et al., 2000). During the late Tithonian, sedimentation was confined to the central part of the basin, which was ringed by irregular embayments with increasingly restricted depositional environments, including some evaporite-bearing deposits (Figs. 3 and 4).

The transition between Late Jurassic deposits and Early Cretaceous deposits is marked in France and England by the presence of extremely heterogeneous and peculiar facies, including oolitic carbonates, evaporites, dolomite, and claystone, termed "Purbeckian facies" (Figs. 2 and 4; Deconinck and Strasser, 1987; Deconinck et al., 1988; Strasser, 1988; Joachimski, 1994; Deconinck et al., 2001). A review of regional lithostratigraphy is made to clearly present the age model applied to the Purbeckian beds and Wealden facies in the sections of the eastern Paris Basin (Fig. 2).

The *Calcaires du Barrois* Formation corresponds to the last significant record (140 m thick) of Jurassic marine carbonates in the Paris Basin during the *elegans* Zone of the early Tithonian (Rusciadelli, 1996; Fig. 2). This formation is subdivided into three members: (1) *Barre lithographique* Member, (2) *Calcaires de Dommartin* (in turn subdivided into four beds *Marnes à Hémicidaris, Pierre Chaline, Oolithe de Bure* and *Calcaires cariés et tachetés*), (3) *Calcaires tubuleux* Member (Mégnien and Mégnien, 1980). These carbonate members are mainly muddy limestones with a few bioclastic sets deposited on a wave-dominated ramp extending from open marine to lagoonal environments (Brigaud et al., 2014). The uppermost surface of these limestones corresponds to a regressive surface called Ti1 (Fig. 2) associated with a main facies change with the first appearance of Purbeck beds composed of dolomitic coastal facies (Rusciadelli, 1996; Hardenbol et al., 1998; Jacquin et al., 1998a). In the eastern Paris Basin, the Purbeckian facies include four formations: (1) the *Dolomie inférieure*, (2) the *Oolithe de Savonnières,* (3) the *Dolomie supérieure,* and (4) the *Dolomie de Saint-Dizier* (Fig. 2). Building stone has been extracted from the *Oolithe de*

Savonnières Formation in quarries since the second half of the nineteenth century (Lorenz and Lehrberger, 2013). The occurrence of dinoflagellates *Egmontodinium polyplacophorum*, *Subtilisphaera inaffecta* and *Pareodinia stegasta* in the *Dolomie inférieure* indicates an early Tithonian age, and more precisely the lower part of the *Wheatleyensis* Zone (Rusciadelli, 1996; Fig. 2). The occurrence of dinoflagellates *Occisucysta balios* and *Senoniasphaera jurassica* in the *Dolomite supérieure* indicates an age not younger than the *Anguiformis* Zone age (late Tithonian; Rusciadelli, 1996; Fig. 2). The *Dolomie supérieure* contains evaporitic facies underlining the regressive trend recorded during the latest Jurassic (Rusciadelli, 1996; Figs. 2 and 4). The upper boundary of the *Dolomie supérieure* corresponds to a major erosional surface in the Paris Basin interpreted as the JCU and the top of the second-order regressive cycle R9 (Fig. 2; Rusciadelli, 1996; Jacquin et al., 1998a).

Pollens, spores, dinoflagellates, and foraminifera do not provide strong biostratigraphic evidence to precisely date the *Dolomie de Saint-Dizier* Formation (=Upper Purbeckian Formation, in Rusciadelli, 1996). Dinoflagellates *Pareodinia brevicornuta* and *Batioladinium* sp. 1, *Cribroperidinium* spp., *Cribroperidinium* spp. and *Dichadogonyaulax culmala* suggest an age ranging from late Tithonian to early Berriasian (Rusciadelli, 1996). Considering the age of the underlying and overlying formations, and the fact that the *Dolomie de Saint-Dizier* Formation onlaps a major unconformity, its age is probably from early Berriasian to early late Berriasian (Rusciadelli, 1996). The major facies change from Purbeck beds carbonate facies to Wealden siliciclastic facies corresponds to the RU, which, like the JCU, illustrates an episode of erosion and/or non-deposition in the Paris Basin (Fig. 2). This surface is interpreted as the upper boundary of the second-order regressive hemicycle R10 (Rusciadelli, 1996; Jacquin et al., 1998b), and is recognizable throughout the Paris Basin (Fig. 2).

The overlying *Sables de Griselles* Formation is composed of continental deposits with eolian sands and plant debris associated with the
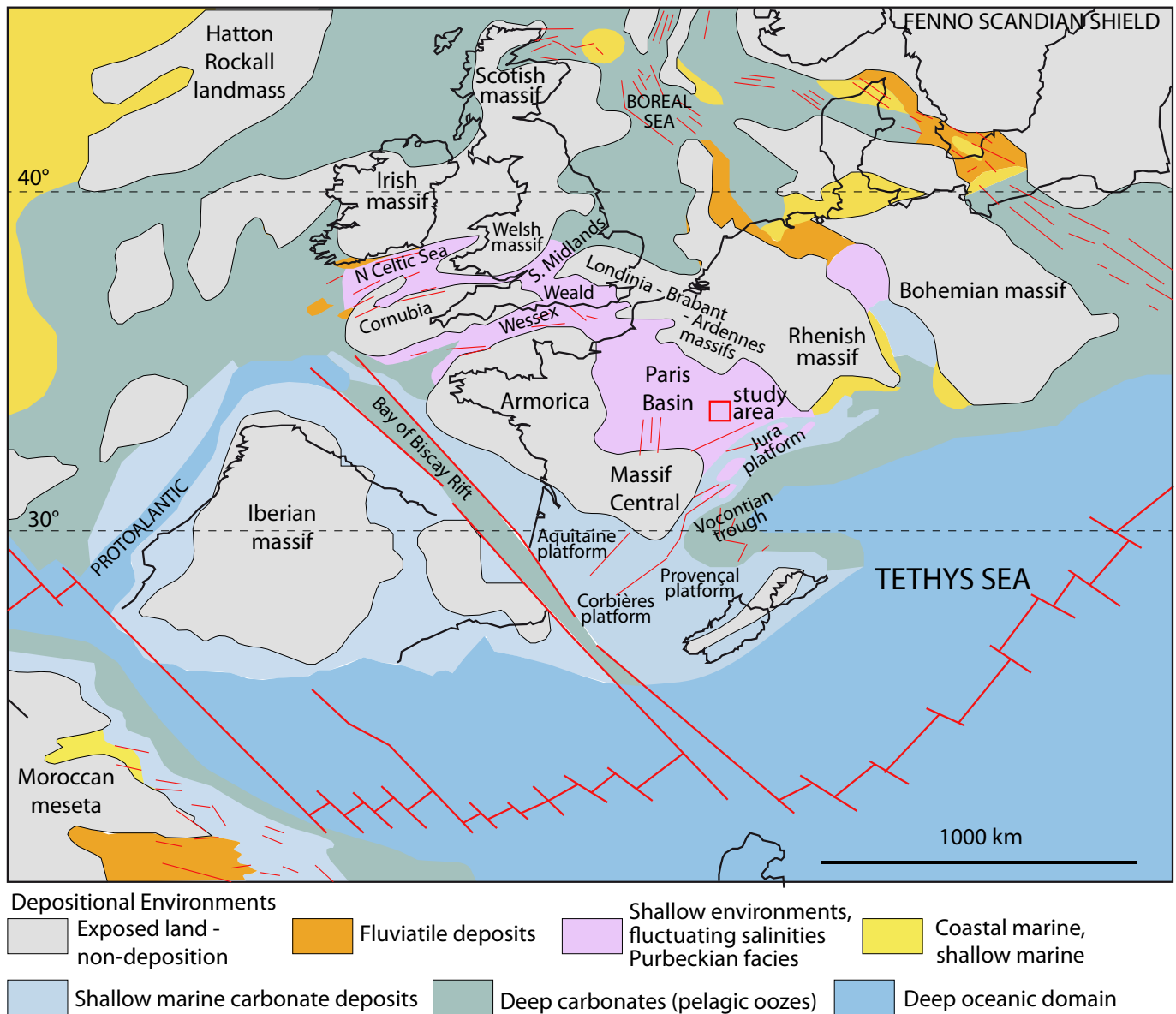
Fig. 3. Location of the study area during the early Tithonian in a paleogeographic reconstruction (based on Enay and Mangold, 1980); (modified from Ziegler, 1988; Thierry and Barrier, 2000).

Wealden facies recognized in the Anglo-Paris Basin (Fig. 3; Mégnien and Mégnien, 1980; Allen and Wimbledon, 1991; Jacquin et al., 1998b). The lower part of the formation locally contains black marls (Fig. 2), which consist of more or less indurated, purplish blue clay sets rich in organic matter (Mégnien and Mégnien, 1980). The presence of dinoflagellates *Theamadinium* of *dodekovae*/*daveyi* group, *Batioladinium* sp. 1, and rare *Muderongia microperforata* or *Cantuladinum spinosum* in these black marls indicates an age between the latest Berriasian (*Stenomphalus-Albidum* Zones) to Valanginian (lower part of Platylenticeras Zone; Fig. 2; Rusciadelli, 1996; Jacquin et al., 1998b). This siliciclastic formation forms the T11/R11 second-order cycle (Jacquin et al., 1998b). The presence of siltite-rich lignite deposits and the occurrence of freshwater spores of *Botryococcus* spp. and *Densoisporites* spp. demonstrate a continental influence, but some minor records of marine microfossils also illustrate spurts of marine influence (Rusciadelli, 1996). These sandy sediments deposited in fluvio-deltaic systems unconformably overlie the Purbeckian facies and sometimes directly cover the early Tithonian *Calcaires du Barrois* (Rusciadelli, 1996). Locally, they contain ferruginous weathering products forming iron sandstones, iron ooids, or centimetric iron crust, mainly of goethite, and in association with

kaolinitic paleosoils (Meyer, 1976; Thiry et al., 2006; Fizaine, 2012). Iron ore was extracted from paleokarstic cavities perforating the *Calcaire du Barrois* Formation at Poisson in the nineteenth century (Mélaire mines, Thiry et al., 2006; Fizaine, 2012). Iron-rich sandstones in the lower part of *the Sable de Griselles* (Valanginian) are also described in the Montiers-sur-Saulx forest (Fizaine, 2012). The *Sables de Griselles* are capped by the Valanginian Unconformity (VU), which is not observable in the studied outcrops.

3. Material and methods

3.1. Sedimentology and sequence stratigraphy

In order to define the depositional environments, a classical facies analysis workflow including a description of lithology, texture, bedding pattern, sedimentary structures, and faunal content, was carried out on eight outcrop sections (Fig. 1). Ninety-five samples were collected and 44 polished thin sections, half-stained by alizarin potassium ferricyanide, were made to investigate microfacies and diagenetic features. Following the definition of Catuneanu et al. (2011), sequence
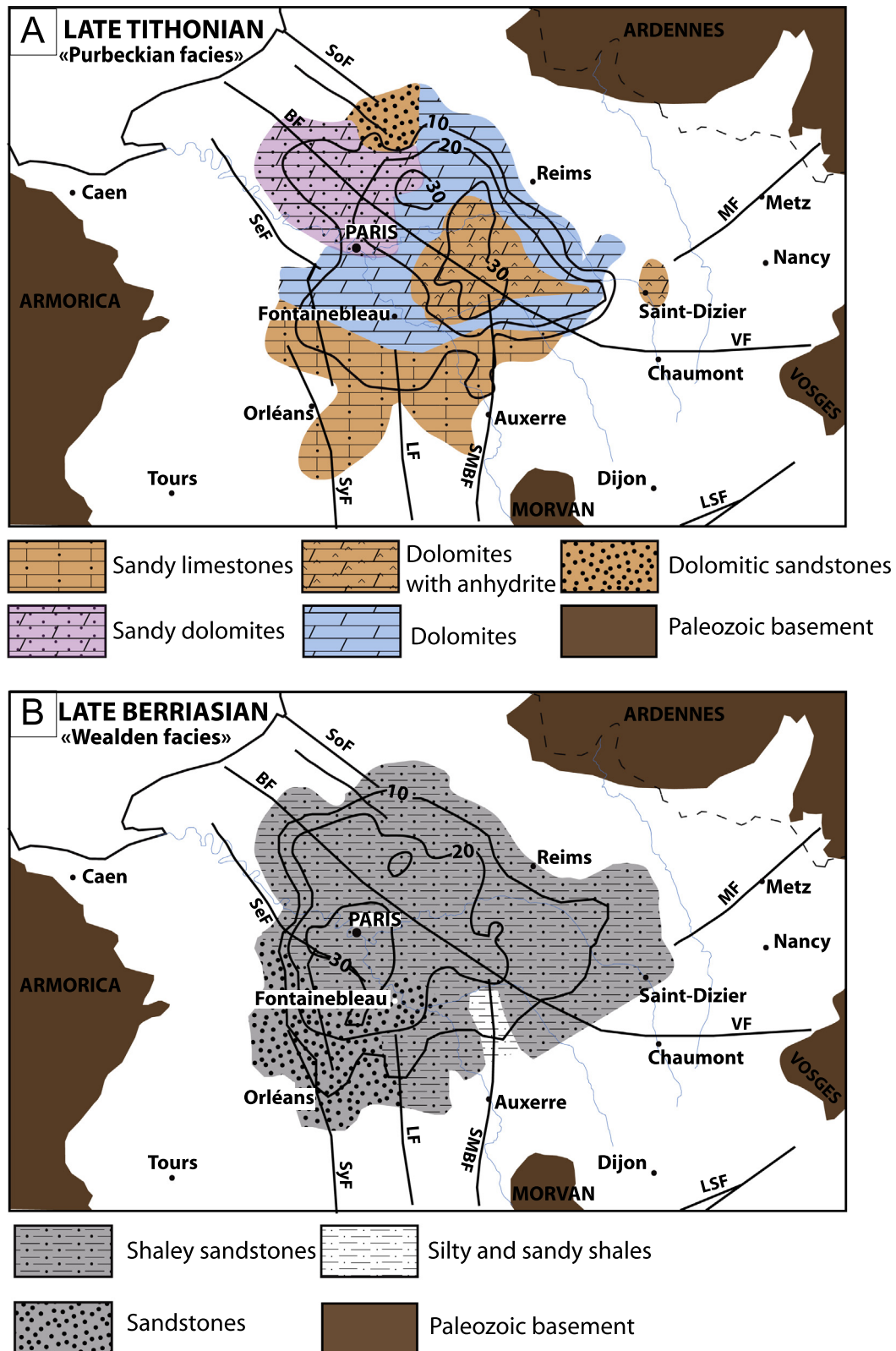
Fig. 4. Facies maps of the Paris Basin during (A) the late Tithonian and (B) the late Berriasian (modified from Mégnien and Mégnien, 1980; Rusciadelli, 1996).

stratigraphic interpretations were performed, integrating data from two additional wells and two previously published quarry descriptions (Fig. 1). Depositional sequences composed of transgressive and regressive systems tracts (TSTs and RSTs) are bounded either by subaerial unconformities (SU), or by maximum regressive surfaces (MRS) when no evidence of exposure is observed. Maximum flooding surfaces (MFS) mark the boundary between deepening-upward to shallowing-upward trends. Subaerial unconformities or maximum regressive surfaces correspond to sequence boundaries (SB), labeled following the definition of Hardenbol et al. (1998). This sequence stratigraphic

work is an essential step in constraining the pattern of development of the sedimentary architectures.

3.2. Decompacted depth, accommodation, subsidence, and tectonic subsidence calculation

The methodology described by Andrieu et al. (2016) is adopted in this study to calculate decompacted sediment thickness, accommodation, subsidence, and tectonic subsidence. Decompacted depth, also called total subsidence, corresponds to the thickness of sediments after decompaction (Steckler and Watts, 1978; Allen and Allen, 2005). Considering that the formations of the Jurassic/Cretaceous boundary were buried to a maximum depth of 300 m (Blaise et al., 2014), the following compaction factors were used for the entire sedimentary series: 1.2 for grainstones, 1.5 for packstones, 2 for wackestones, 2.5 for calci-mudstones, and 3 for marls (Hillgärtner and Strasser, 2003).

Accommodation space can be defined as the sum of the decompacted thicknesses of sediments and of paleodepth variations (Robin et al., 2000). For each facies, paleodepths were estimated based on the examination of sedimentary structures and faunal content. A classic wave zonation was used, considering depths of 10–15 m for the fair-weather wave base and 40 m for the storm wave base (Sahagian et al., 1996; Plint, 2010).

Subsidence corresponds to the increase in accommodation that is not due to eustasy but created instead by basement movements. It was calculated by subtracting eustasy variations from accommodation using the eustasy curve of Haq (2014, 2018).

Tectonic subsidence is independent of isostatic adjustment due to sediment deposition or paleodepth variations. It was calculated using the equation of Steckler and Watts (1978):

$$Y = S\left(\frac{\rho m - \rho b}{\rho m - \rho w}\right) - \Delta SL\left(\frac{\rho m}{\rho m - \rho w}\right) + Wd$$

Y is tectonic subsidence, ρm is mantle density, ρb is mean sediment density, ρw is water density, ΔSL is eustasy variation, and Wd is paleodepth variation. Mean densities of 3.3 g·cm^{-3}, 2.6 g·cm^{-3}, and 2.4 g·cm^{-3} were used for mantle rocks, carbonates, and marls respectively.

Decompacted sediment thickness, accommodation, subsidence, and tectonic subsidence values were calculated for each semicycle (transgressive systems tracts and regressive systems tracts).

Uncertainties in accommodation, subsidence, and tectonic subsidence calculation may be due to uncertainties in the estimates of (1) the eustatic variations by Haq (2014, 2018) for subsidence and tectonic subsidence calculations only, (2) the age model of the sections, (3) the decompacted sediment thickness, (4) paleodepth estimation from facies observations and characterizations. Estimated ages of each sequence boundary and maximum flooding surface are based on the regional biostratigraphy of the sedimentary formations (Rusciadelli, 1996) and on the biozone boundaries from the GTS2012 (Gradstein et al., 2012), the latter being used to calibrate the calculated curves against an accurate age model. The age model applied to the Purbeckian facies and Wealden facies is determined by dinoflagellate cysts found in the eastern Paris Basin sections (Rusciadelli, 1996, Fig. 2). Dinocyst zonations have been developed for the North Sea and their datums calibrated to ammonite zones of the Boreal realm (Hardenbol et al., 1998). Finally, Jurassic boreal ammonite zonations and corresponding ages from GTS2012 (Gradstein et al., 2012) have been used to obtain the duration of stratigraphic intervals. Sedimentary thickness of each TST and RST for three sections (La Fontaine, La Houpette and Poisson) was converted into time to estimated duration of system tracts. Uncertainties in the decompacted sediment thickness depend on the chosen compaction law (Hillgärtner and Strasser, 2003). Uncertainties in paleodepth estimates are 30 m ± 10 m for the upper offshore, 10 m ± 5 m for the shoreface and the lagoon, and 5 m ± 5 m above sea

level for continental environments. An additional ±5 m uncertainty was used to take into account the reading precision of the curve by Haq (2014, 2018). Calculated values are rounded to the nearest 10 m.

3.3. Diagenesis and stable isotopes

Diagenesis was studied using optical microscopy on thin sections completed by cathodoluminescence observation with an 8200MKII Technosyn (15 kV and 300 mA) coupled to an Olympus microscope and a Qicam Fast 1394 digital camera. Cement stratigraphy and diagenetic sequencing were established on the basis of superimposition and cross-cutting relationships from thin-section observations. Visual estimations of the proportion of the cement stages were carried out on the 44 thin-sections. The diagenetic log method proposed by Durlet et al. (1992), specifically designed to supplement the partial sedimentary record, is used to represent the paragenesis of the studied samples in relationship to unconformities.

Stable carbon and oxygen isotopes ($\delta^{18}O$ and $\delta^{13}C$) were used to ascertain the isotopic signal of bulk rock in different depositional environments. Carbonate ($n = 57$) was sampled using a dental micro-drill with a diameter of 1 mm. Carbonate powder was reacted with 100% orthophosphoric acid at 25 °C during 4 h and the derived CO_2 was analyzed using a VG Sira 10 mass spectrometer to determine O and C isotope composition of calcite at the GEOPS laboratory (Université Paris-Sud, Orsay). Fifteen powder samples composed of carbonate mixtures were analyzed using the selective extraction technique for isotopic analysis of coexisting calcite and dolomite described in Al-Aasm et al. (1990). Carbonate powder was first reacted with 100% orthophosphoric acid at 25 °C during 4 h, the composition of the extracted CO_2 was analyzed using a VG Sira 10 mass spectrometer to determine O and C isotope composition of calcite. The vessel is then close and the reaction is continued for 20 h at 25 °C after which time the released CO_2 is removed. The samples may then be allowed to react 50 °C and the CO_2 subsequently extracted is used to determine the isotopic composition of dolomite. All isotopic values are reported in the standard δ-notation in per mil relative to V-PDB (Vienna Pee Dee Belemnite) by assigning a $\delta^{13}C$ value of $+1.95‰$ and a $\delta^{18}O$ value of $-2.20‰$ to NBS19. Reproducibility was checked by replicate analysis of laboratory standards and was ±0.2‰ for oxygen isotopes and ±0.1‰ for carbon isotopes.

4. Results

4.1. Sedimentary facies

A sedimentological log in La Fontaine quarry is chosen as a reference to illustrate the Late Jurassic/Early Cretaceous stratigraphic succession and the associated depositional environments (Fig. 5). For the entire stratigraphic interval studied, the facies analysis is used to define five depositional environments ranging from upper offshore to fluvial-deltaic environments (Fig. 6). Observations and descriptions are summarized in Table 1.

4.1.1. Upper offshore storm-dominated environment (facies association FA1)

This facies association is characterized by marl-limestone alternations. Based on stacking patterns and dominant allochems in limestones, two lithofacies are identified: (1) alternations of decimeter-thick marl layers and decimeter-thick calci-mudstone layers (lithofacies LF1a, Fig. 7A-B), and (2) alternations of decimeter-thick marl layers and decimeter-thick bioclastic wackestone beds (lithofacies LF1b, Fig. 7B). In lithofacies LF1a, the calci-mudstone contains very fine sponge spicules and comminuted fragments of bivalves, brachiopods, or echinoderms. The lower part of the limestone beds in lithofacies LF1b contains bivalve debris, brachiopod shells, and echinoderm fragments, forming graded layers and probably illustrating storm deposits. Sedimentation occurred
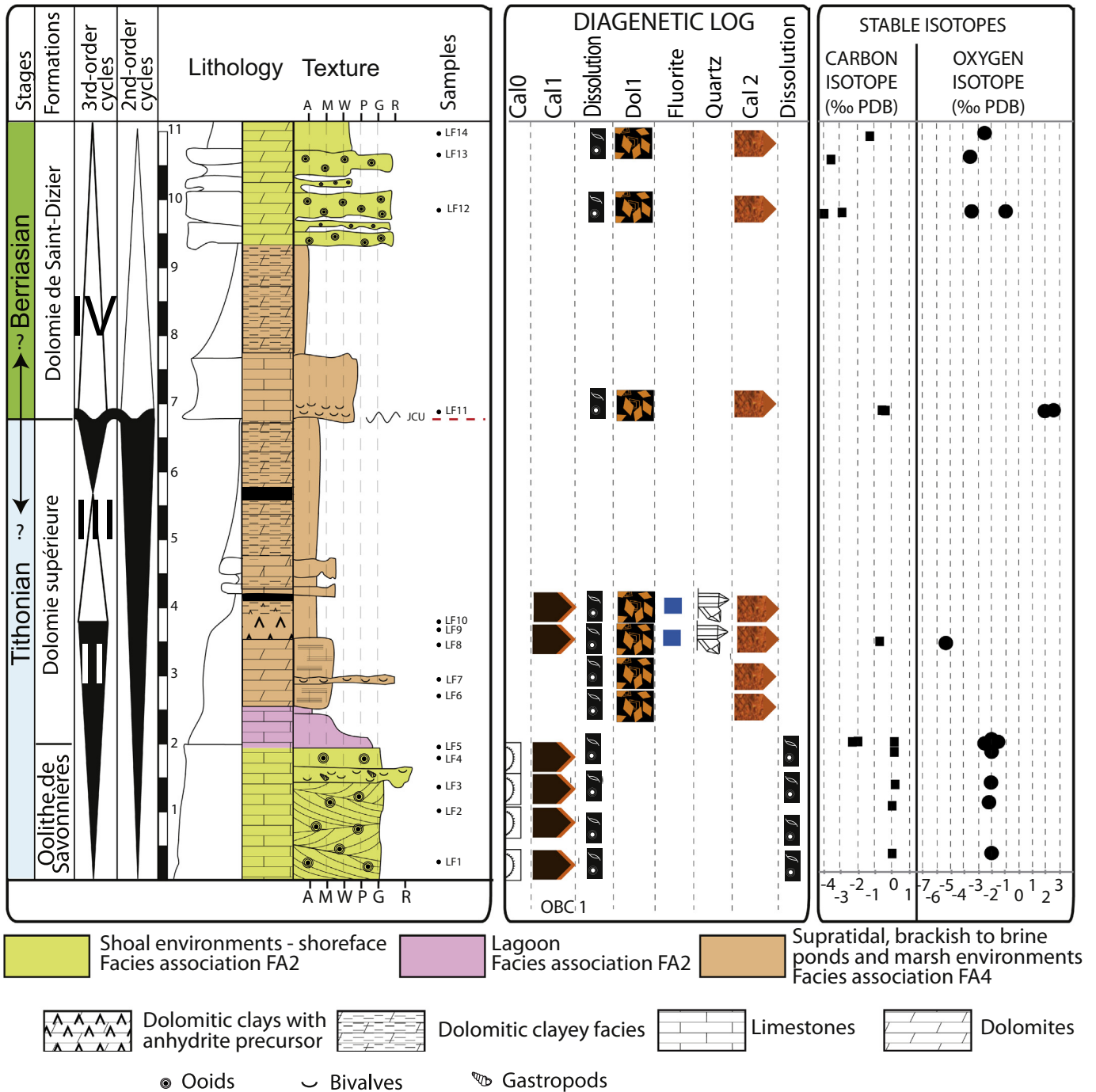
Fig. 5. Sedimentological log of La Fontaine quarry section with geological stages, lithostratigraphy, sequence stratigraphy (3rd-order sequences), lithology, texture, diagenetic stages, and stable isotopes.

in a very quiet setting that was only disturbed during storm episodes, suggesting a depositional environment between the storm wave base and the fair-weather wave base (Fig. 6).

4.1.2. Shoal environment, ooid or skeletal-dominated facies (facies association FA2)

In this dominantly grain-supported facies association, three main lithofacies are distinguished: (1) an ooid grainstone (lithofacies LF2a, Fig. 8A-B), (2) a bioclastic grainstone to rudstone (lithofacies LF2b, Fig. 8C), and (3) an oo-bioclastic grainstone to rudstone (lithofacies LF2c, Fig. 8D). The skeletal grains may include bivalves, echinoderms, gastropods, brachiopods, bryozoans, and green algae in variable proportions suggesting well oxygenated water with normal salinity.

Common sigmoid cross-beddings and grainstone/rudstone sandwaves indicate shallow high-energy wave-dominated conditions, in a shoreface environment (Fig. 8F). Locally, herring-bone stratifications can be observed, as well as small scale vertical alternation between muddy horizons and coarse-grained facies with current ripples and lenticular bedding, which suggest a tidal influence (Fig. 8E, G).

4.1.3. Lagoon and intertidal environments (facies association FA3)

Two lime mud dominated lithofacies form this association: (1) fibro-radial ooid packstone (lithofacies LF3a, Fig. 9A), and (2) a peloidal calci-mudstone/wackestone (lithofacies LF3b, Fig. 9B). The dominance of mud-supported textures indicates low-energy conditions. In the facies association FA3, the fauna is mainly composed of benthic
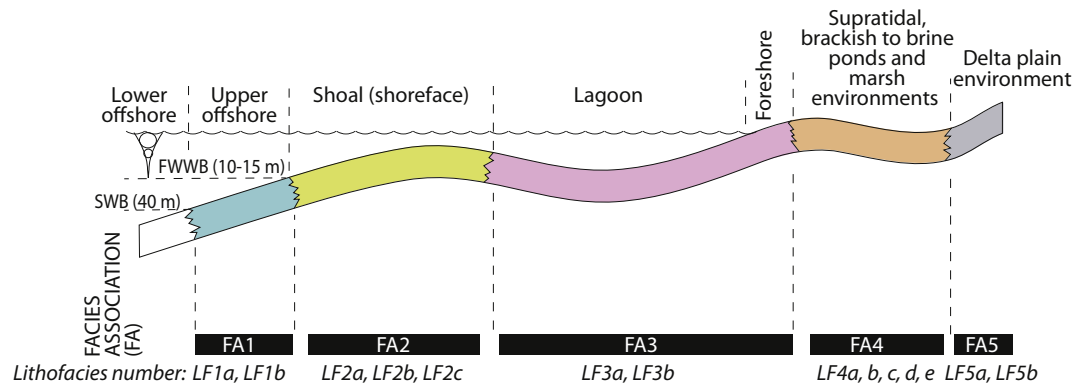
Fig. 6. Location of the Tithonian to Valanginian facies distribution on a downdip profile from the upper offshore to fluvio-deltaic environment in the eastern Paris Basin. The range of variation of the fair-weather wave base and storm-wave base depths are estimated by Sahagian et al. (1996) and Plint (2010).

foraminifera, echinoderm fragments, bivalves, and gastropods. In these mud-supported facies, the presence of peloids, very well-preserved gastropods, and planar stratifications are indicative of a protected lagoonal environment (Fig. 6). The scattered grain-supported layers correspond to either local tidal deposits (channels, bars), or storm-washover deposits.

Table 1

Position on the downdip profile, lithofacies, non-bioclastic and bioclastic components, sedimentary and biogenic structures, sorting, granulometry, and energy and depositional environment.

Position within the downdip profile (hydrodynamism)	Lithofacies (LF)	Composition 1- Non-skeletal 2- biota	Sedimentary and biogenic structures	Sorting and grain size	Energy and depositional environment
Upper offshore Storm-dominated environment Paleodepth 10–40 m (Facies association FA1)	LF1a – marl/calci-mudstone alternations	1- silts (C) 2- bivalves (F), brachiopods (C), echinoderms (C), demosponges spicules (F)	storm-graded layers abundant bioturbation	<10 μm to 1 cm poorly sorted	low to moderate energy distal upper offshore
	LF1b – marls/bioclastic wackestone alternations	1- silts (C) 2- bivalves (F), brachiopods (C), echinoderms (C)	storm-graded layers abundant bioturbation	<10 μm to 1 cm poorly sorted	low to moderate energy distal upper offshore
Shoal environment – Shoreface ooid or skeletal-dominated facies Paleodepth <30 m (Facies association FA2)	LF2a - ooid grainstone	1- ooids (A), intraclasts (R) 2- bivalves (R), crinoids (R), green algae (R), gastropods (R), brachiopods (R), bryozoans (R),	sigmoid cross-bedding herring-bones stratifications	200 μm to 500 μm; very well sorted	high energy, wave or tidally dominated, shoreface
	LF2b - bioclastic grainstone to rudstone	1- peloids (A), oncoids (C), intraclasts (R) 2- bivalves (C), echinoderms (C), bryozoans (R), brachiopods (R), gastropods (C),	sigmoid cross-bedding	100 μm to 500 μm; very well sorted	high energy, wave dominated, shoreface
	LF2c- oo-bioclastic grainstone to rudstone	1- ooids (F), peloids (R) 2- echinoids (C), bivalves (A)	cross-bedding in dunes alternations between current ripples or lenticular bedding and mud beds herring-bones stratifications	200 μm to 3 mm; poorly sorted	high energy, wave or tidally dominated, shoreface
Lagoon and intertidal environments Paleodepth <30 m (Facies association FA3)	LF3a – fibro-radial ooid packstone	1- ooids (A), peloids (R) 2- bivalves (C), gastropods (C), benthic foraminifera (R), echinoderms (R)	planar-bedding, thin argillaceous intercalations	50 μm to 1 cm very poorly sorted	low to moderate energy restricted and protected environments
	LF3b – peloidal calci-mudstone/wackestone	1- peloids (A), oncoids (F), ooids (F), 2- bivalves (C), gastropods (C), benthic foraminifera (R), echinoderms (R)	planar-bedding, thin argillaceous intercalations	50 μm to 1 cm very poorly sorted	low to moderate energy restricted and protected environments
4 Supratidal, brackish to brine ponds and marsh environments (Facies association FA4)	LF4a - microbially laminated calci-mudstone to packstone facies with peloids	1- peloids (A), intraclasts (F) 2- bivalves (R), gastropods (R)	peloidal structures microbial laminae birdseyes	10-50 μm well-sorted	supratidal low energy
	LF4b - dolomicrite	1- peloids (A), intraclasts (R), 2- bivalves (C) gastropods (F)	birdseyes	<10 μm of fine grained dolomites	emersive facies Dolomite marshes Episodic influx of normal marine waters
	LF4c - dolostone	1- peloids (A), medium-size (10-100 μm) dolomite crystals (A), bivalves (C)		10-100 μm dolomite spar	dolomite marshes episodic influx of normal marine waters
	LF4d - dolomitic clayey facies				very low energy dolomite marshes episodic influx of normal marine waters
	LF4e – Dolomitic clays or muds with silicified nodules of anhydrite precursor		centimetric silica nodules quartz cauliflower or rosette textures collapses breccias dissolution of evaporite minerals		brine ponds
Delta plain environment (Facies association FA5)	LF5a –Sands and sandstones	1- quartz sand and silts, Goethite cements		Fine to coarse sand well-sorted	sand bar of distributary-channels
	LF5b – Organic-rich silt layers	1- silts	organic matter		swamp environments between distributary channels
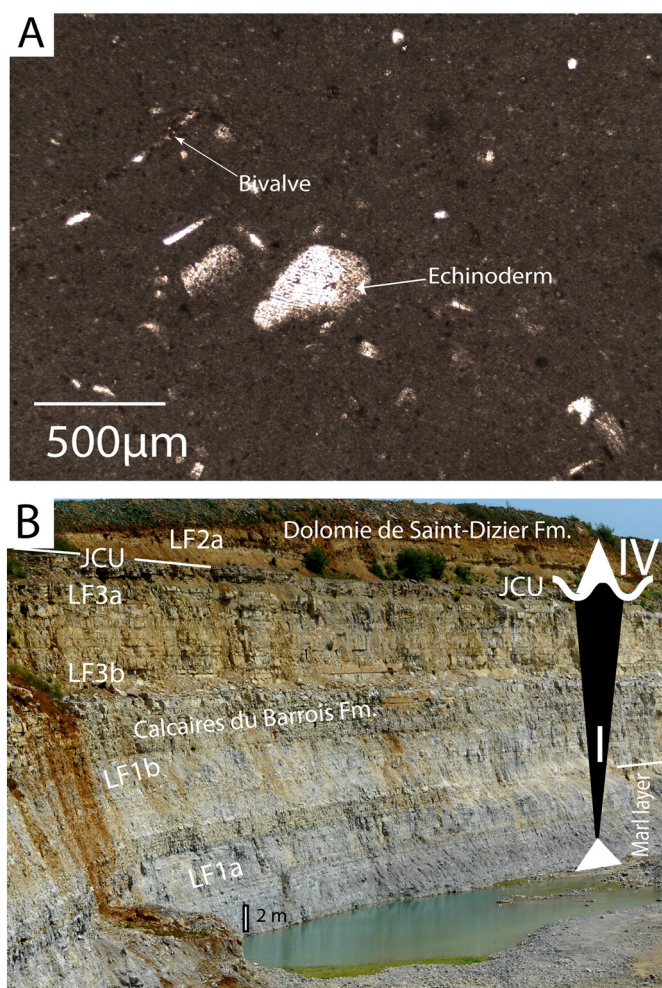
Fig. 7. A- Calci-mudstone with echinoderms and fine bivalves, Lithofacies LF1a, sample G2, Givrauval quarry, *Calcaire du Barrois* Formation. B- Magneux quarry showing the *Calcaire du Barrois* and *Dolomie de Saint-Dizier* Formations. In the *Calcaire du Barrois Formation*, marl-limestone alternations with LF1a and LF1b, and LF3b and LF3a are located in Sequence I. Notice the unconformity JCU between Sequences I and IV.

4.1.4. Supratidal, brackish to brine ponds and marsh environments (facies association FA4)

Facies association FA4 consist of five lithofacies: (1) a laminated calci-mudstone to packstone facies with peloidal texture (lithofacies LF4a, Fig. 10A), (2) a laminated dolomicrite facies with peloids and *birdseyes* (lithofacies LF4b, Fig. 10B–D), (3) a dolomicrosparite to dolosparite facies with peloids (lithofacies LF4c, Fig. 10E), (4) an argillaceous dolomite facies with peloids (lithofacies LF4d, Fig. 10D), and (5) dolomitic clays containing decimeter-thick laminated calcareous calci-mudstone facies with silicified nodules (lithofacies LF4e, Fig. 10D, F–H). Lithofacies LF4a consists of alternations between microbially laminated calci-mudstone layers and coarse bioclastic (gastropods and bivalves) wakestone/packstone layers with *birdseyes*, which are indicative of intertidal environments with ephemeral exposures (Figs. 6 and 10A). Silicified nodules in dolomitic facies are common in sabkhas and supratidal settings (Simone et al., 2012). Silica nodules form centimeter-scale geodes (Figs. 10D and 11C) with cauliflower or rosette textures (Fig. 10H), which is a typical feature observed after the replacement of anhydrite in evaporite-bearing rocks (Arbey, 1980). Associated with silicified nodules, some layers with microbial laminations display entherolitic folds characterized by centimeter-thick antiform structures (Fig. 11C). These structures possibly result from the deformation of sediments during crystallization of gypsum. Collapse breccias and evaporite dissolution breccias are observed in lithofacies LF4e revealing

plastic deformation (Fig. 11A–B). Evidence for evaporite precursors and associated features (collapse breccias), dolomite with all the petrographic aspects of early dolomitization processes (see discussion), and microbial laminations together suggest deposition in sabkha-like environments and/or in restricted evaporative ponds or salt marshes in supratidal environments and under semi-arid conditions (Fig. 6).

4.1.5. Delta plain environment (facies association FA5)

Two lithofacies are distinguished in facies association FA5: (1) a fine and well-sorted sandstone (facies LF5a, Fig. 12A, C–D), and (2) an organic matter-rich layered siltstone (Fig. 12D). Lithofacies LF5a corresponds to fine and well-sorted quartzarenite devoid of fauna (Fig. 12A–C, E). The absence of bioclasts and the repeated occurrence of sand lags above erosional surfaces suggest incision and migration of fluvial channels in a delta plain environment (Figs. 6 and 12C). The occurrence of layers with high organic content is indicative of sedimentation in quiet zones, possibly swamps between distributary channels.

4.2. Stratigraphic architecture

Five depositional sequences are identified along the studied stratigraphic interval (Fig. 13). Considering a time range of about 15 My for the whole interval, the rough estimate of the average duration for each cycle is 3 My (Gradstein et al., 2012), which is in the range of duration for third-order cycles (1 to 10 My; Schlager, 2004). These cycles are organized into three lower order transgressive-regressive cycles, likened to second-order cycles and labeled regressive cycle R9, Transgressive-regressive cycle T10-R10, and transgressive-regressive cycle T11-R11 (Fig. 2). The latter low order cycles are defined by Jacquin et al. (1998a); Jacquin and de Graciansky (1998b) in the Paris Basin and other western European Basins.

4.2.1. Tithonian sequences (Sequences I, II, and III)

Sequences I, II, and III form the regressive hemicycle R9 *sensu* Rusciadelli (1996) and Jacquin et al. (1998a). The maximum flooding surface of Sequence I is located in a thick marl succession at the base of the Magneux section (Figs. 7C and 13). The regressive systems tract of this sequence marks an evolution from upper offshore facies (lithofacies LF1a) to lagoonal oolitic packstone (lithofacies LF3a, Figs. 7C, 9A). The top of the *Calcaire du Barrois* locally exhibits root traces as in the Magneux quarry and corresponds to a subaerial exposure surface named Ti1 (Figs. 7C and 13). The upper part of Sequence I is observed all along the reference transect (Fig. 13).

The transgressive systems tract of Sequence II is composed of 8 m-thick dolomitic facies (LF4b and LF4c) and oolitic or bioclastic grainstone (facies association FA2) of the *Oolithe de Savonnières* (Figs. 8E–F, 13). The maximum flooding surface of Sequence II corresponds to the facies association FA2 (Fig. 13). The regressive systems tract of Sequence II is characterized by the development of lagoonal calci-mudstone (lithofacies LF3b), followed by microbially laminated dolomitic facies (facies association FA4, Figs. 10B, D and 11A). The upper part of Sequence II corresponds to the dolomitic facies with silicified nodules deposited in sabkha-like environments (lithofacies LF4e, Figs. 10D and 11A). This regressive systems tract is covered by the Ti3 sequence boundary in the middle part of the *Dolomie supérieure* and identified by the development of silicified nodules (Fig. 13). Sequence II is recorded in the La Fontaine, Longue Queue, Champ Maillot, La Couleuvre, and Terme sections and in the 216-VT and 219-VT boreholes (Fig. 13).

The transgressive systems tract of Sequence III is characterized by a 2 m-thick dolomitic deposit, corresponding to the upper part of the *Dolomie supérieure*. Claystone levels in this succession mark the maximum flooding surface. The regressive systems tract corresponds to a 1 m-thick dolomitic succession at La Fontaine quarry (Figs. 11A and 13). Sequence III is observed in the La Fontaine, Longue Queue, Champ Maillot, La Couleuvre, and Terme quarries and in the 216-VT borehole.
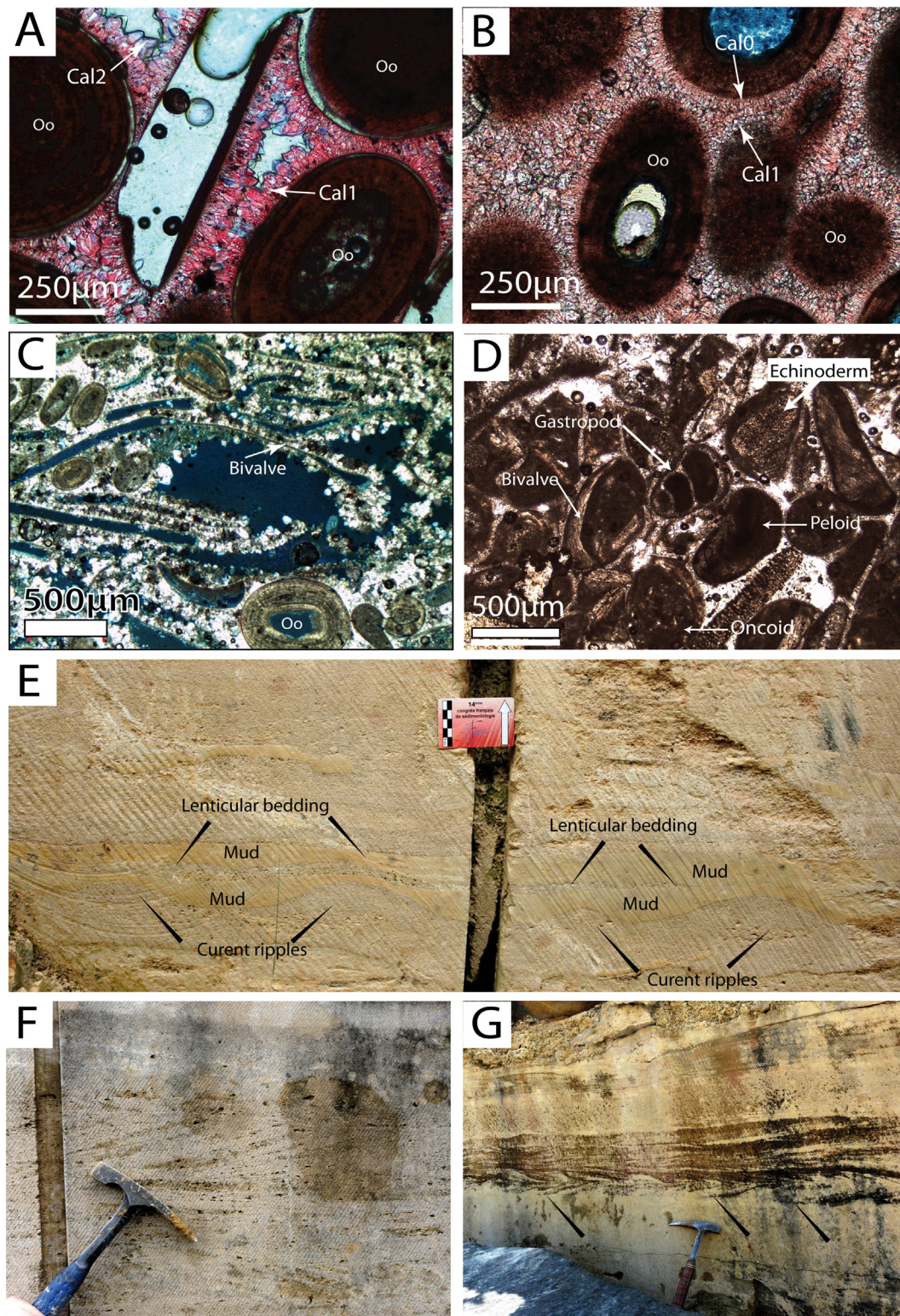
Fig. 8. A- Ooid (Oo) grainstone facies with Calcite 1 (Cal1) and Calcite 2 (Cal2) stages, Lithofacies LF2a, sample LF2, La Fontaine quarry, *Oolithe de Savonnières* Formation. B- Ooid grainstone facies with Calcite 0 (Cal0) and Calcite 1 (Cal1) stages, Lithofacies LF2a, sample LQ14, La Longue Queue quarry, *Oolithe de Savonnières* Formation. C- Oo-bioclastic rudstone, Lithofacies LF2c, sample LQ17, La Longue Queue quarry, *Oolithe de Savonnières* Formation. D- Bioclastic grainstone, Lithofacies LF2b, sample G1, Givrauval quarry, *Oolithe de Bure* Member. E- Lenticular bedding, current ripples of ooid grainstone and mud facies alternation suggesting tidal dynamics. F- Cross-trough bedding forming dunes in Lithofacies LF2c in the La Fontaine quarry, *Oolite de Savonnières* Formation G- Herring bones (arrows) in the Champ Maillot quarry, *Oolithe de Savonnières* Formation.

4.2.2. The early Berriasian sequence (Sequence IV)

The transgressive hemicycle of Sequence IV is characterized by a change from dolomitic facies (LF4b and 4c) to oolitic and bioclastic grainstone (LF2c, Figs. 11A and 13). The LF2c facies comprises a high concentration of bioclasts, ooids, and peloids, illustrating the return of marine conditions and corresponding to the maximum flooding surface of Sequence IV. The regressive systems tract consists of 2 m-thick dolomitic facies. Sequence IV is capped by the second-order Ryazanian
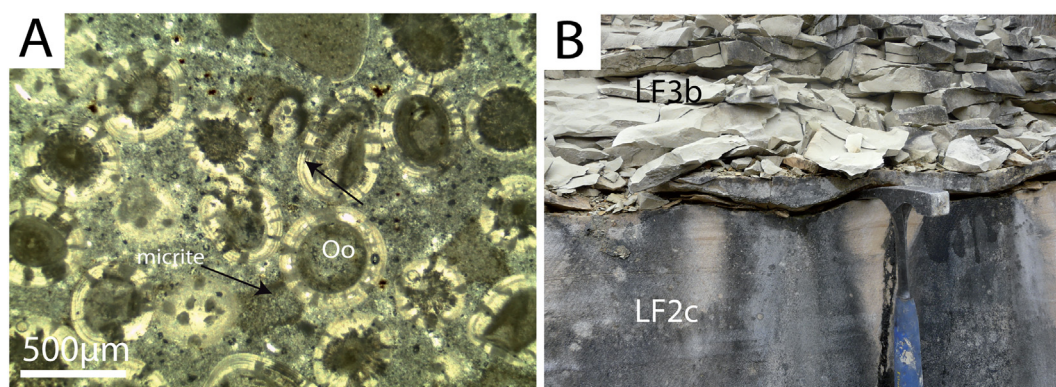
Fig. 9. A- Fibro-radial ooid packstone, Lithofacies LF3a, sample M-2, Magneux quarry, *Calcaire du Barrois* Formation. B- Facies transition between peloidal calci-mudstone/wackestone (Lithofacies LF3b) and ooid facies (Lithofacies LF2a), upper part of the *Oolithe de Savonnières* Formation, La Fontaine quarry. Notice the current ripples at the transition.

Unconformity (RU), corresponding to an erosion surface evidenced by incised valleys (Rusciadelli, 1996). The differential erosion observed in association with the RU may be linked to karstification and/or fluvial erosion during the deposition of the following fluvial clastic deposits.

4.2.3. The late Berriasian to early Valanginian sequence (Sequence V)

Only the beginning of Sequence V, formed by the *Sables de Griselles*, is observed in detail (Fig. 13), and corresponds to fluvial sands (facies LF5a), locally iron sandstones (Terme, Fig. 12E–F) and organic matter-rich layers (facies LF5b). This sequence rests unconformably above the underlying deposits, down to the top of Sequence II in borehole 219-VT and top of Sequence 1 at Poissons (Fig. 13). A large sedimentary gap is identified, with most of the upper Berriasian missing (Rusciadelli, 1996). Ferruginous products (iron sandstones, iron ooids, or centrimetric iron clumps) attributed to the Early Cretaceous, filling paleokarstic cavities at the top of the *Calcaire du Barrois* Formation at Poissons, suggest weathering processes during exposure associated to RU and probably JCU which are merged at Poissons section (Mélaire mines, Thiry et al., 2006; Fizaine, 2012, Fig. 13). Unconformities JCU and RU are also merged at Champ Maillot, Terme, and core 219-VT.

4.3. Diagenetic characteristics

Four diagenetic phases were identified in the carbonate deposits: (1) isopachous fibrous cements (Calcite 0), (2) scalenohedral or rhombohedral calcite cement (Calcite 1), (3) replacement of aragonitic shells by blocky calcite, (4) dolomite, including replacive texture (of calcitic ooids for example) and cement stages, (Dolomite 1 and 2). A local level, containing silica nodules, displays a particular paragenetic sequence marked by (1) fluorite, (2) geodic quartz including replacement of gypsum/anhydrite precursors by quartz, and (3) blocky calcite (Calcite 2). Sandstone facies are marked by goethite intergranular cements. These diagenetic stages are placed on the sedimentary logs on Fig. 5 (except goethite), and ordered in a paragenetic sequence (Fig. 14).

4.3.1. Isopachous fibrous calcite (Calcite 0 – Cal0)

This cement is non-ferroan and forms a very fine (<5 μm, Fig. 15B, D) to medium (10–30 μm, Fig. 8A–B) isopachous fibrous fringe around carbonated grains (bioclasts, ooids, peloids). The cloudy orange luminescence of these fringes is typical of recrystallization of a high magnesium calcite (HMC) precursor into low magnesium calcite (LMC; Durlet and Loreau, 1996; Andrieu et al., 2018). This kind of cement is only observed in the *Oolithe de Savonnières* Formation, within the facies association FA2 (Fig. 14).

4.3.2. Scalenohedral or rhombohedral calcite cement (Calcite 1 - Cal1)

These cements appear either as scalenohedral or rhombohedral clear non-ferroan calcite. The scalenohedral-shaped cement develops

either immediately around grains or after the isopachous fibrous fringes in the case of the *Oolithe de Savonnières*, and forms 20–30 μm-thick fringes with a faint dogtooth fabric, partially filling interparticle pores (Fig. 15B, D). Faint dogtooth cements are only found in the *Oolithe de Savonnières* in facies association FA2 (Fig. 14). The rhombohedral-shaped cement forms 50 μm to 100 μm-thick fringes lining vugs in the *Dolomie supérieure* Formation, within facies association FA4 (Figs. 14 and 15E). These scalenohedral and rhombohedral calcite cements are non-luminescent, with rare very thin internal brighter stripes, and are systematically covered by a late stage orange luminescent subzone (Fig. 15B, D, and E), which suggests possible contemporaneity between the scalenohedral and rhombohedral shapes.

4.3.3. Dissolution

Moldic dissolution of the aragonitic skeletal debris, mostly gastropods and bivalves, and calcitic peloids and ooids occurred in all the studied limestones (Fig. 14). The molds were filled by dolomite (Dol1 and 2) and Calcite 2, probably suggesting an early process. Collapse breccias observed in the dolomitic formation of Sequences II and III may be contemporaneous with this dissolution phase.

4.3.4. Dolomite (Dolomite 1 and 2 – Dol1 and Dol2)

Two dolomite crystallization stages (Dol1 and Dol2), both non-ferroan, are identified in samples from the *Dolomie de Saint-Dizier*, the *Dolomie inférieure* and *supérieure* Formations, and locally in the upper part of the *Oolithe de Savonnières* Formation (Fig. 16A–H). Dolomites are found in facies associations FA2 and FA4 (Fig. 14). The first dolomite Dol1 exhibits fine rhombohedral crystals (<10 μm) with an orange luminescence (Fig. 16A–F), replacing grains (ooids) and micrite matrix in calci-mudstone/wackestone facies (Figs. 11B and 16H). Locally, coarser rhombohedral (10–30 μm) crystals of Dol1 fill interparticle pores (Fig. 16G). The second dolomite Dol2 is medium to coarse crystalline, with crystal sizes ranging between 30 μm and 200 μm, and is definitely a pore-occluding cement (Fig. 16A–F). This clear dolomite is mostly non-luminescent with very fine orange stripes highlighting the growth zones (Fig. 16B, D–F). In the ooid grainstone to rudstone facies of the *Dolomie de Saint-Dizier* Formation, dolomite Dol2 is found in the molds of ooids, illustrating that calcite was dissolved locally during or after Dol1 and prior to Dol2 (Fig. 16G).

4.3.5. Fluorite (Fl)

Fluorite crystals with a typical blue cathodoluminescence consist of 20–50 μm cubes which precipitated in vugs and possibly replaced anhydrite or gypsum crystals within the nodular levels of the *Dolomie supérieure* in facies association FA4 (Figs. 14 and 15H).
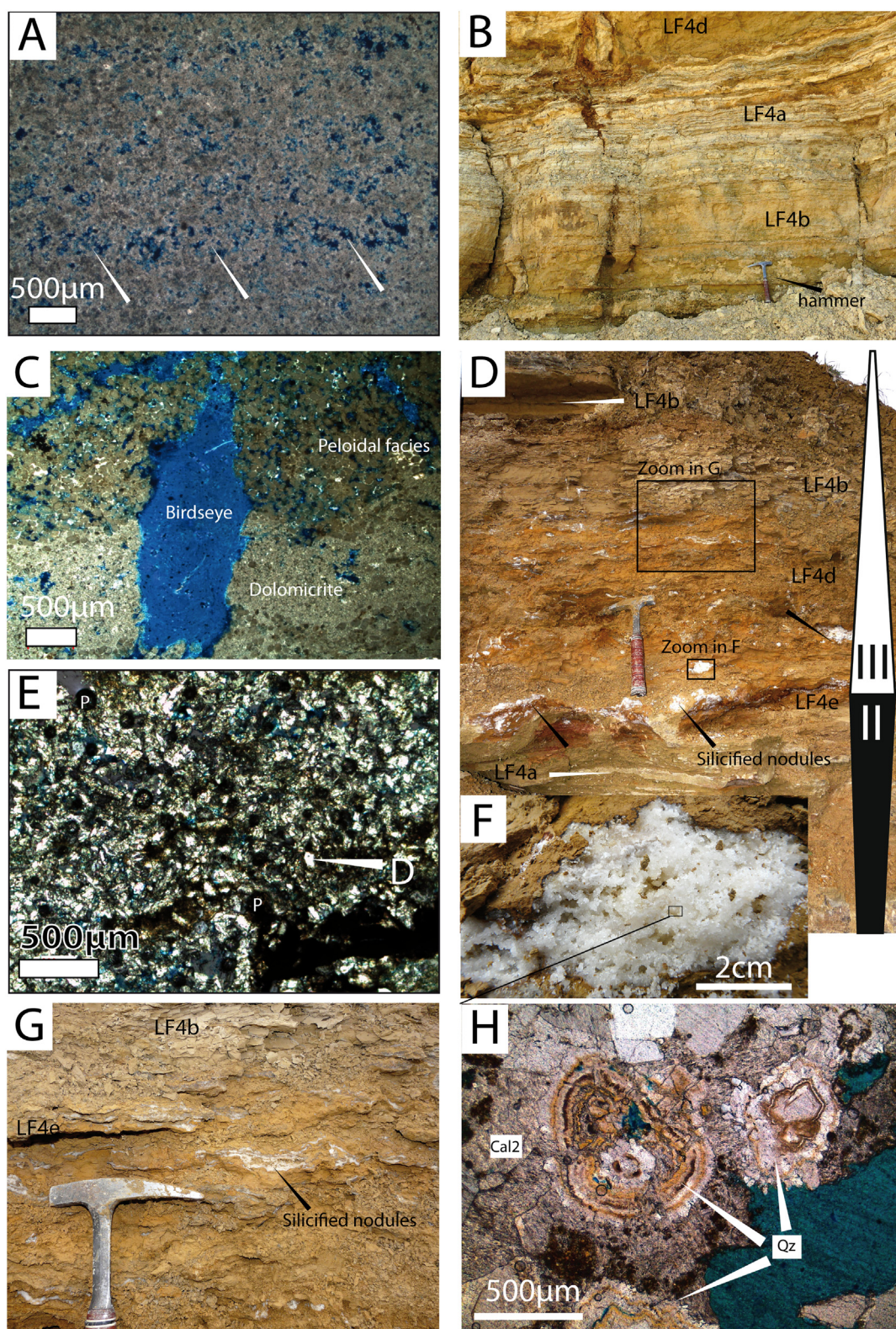
Fig. 10. A- Microbially laminated packstone facies with peloids (Lithofacies LF4a), sample LF6, La Fontaine quarry, *Oolithe de Savonnières* Formation. B- Microbially laminated packstone facies with peloids (Lithofacies LF4a), dolomicrite (Lithofacies LF4b) and dolomitic clays (Lithofacies LF4d), *Dolomie de Saint-Dizier* Formation, Magneux quarry. C- Dolomicrite with fine-grained dolomite crystals (<10 μm) (Lithofacies LF4b) with birdseyes and peloids, sample LQ12, Longue Queue quarry, *Dolomie supérieure* Formation. D- Outcrop of the *Dolomie supérieure* Formation in the La Fontaine quarry showing the dolomitic clays or muds with silicified nodules of anhydrite precursor (Lithofacies LF4e), microbially laminated calci-mudstone (LF4a), dolomicrite (LF4b) and dolomitic clays (LF4d). Note the zoom location of silicified nodules (zoom microphotograph in F and G). E- Dolostone composed of 40–50 μm dolomite spars and peloids (Lithofacies LF4c), sample LQ11a Longue Queue quarry, *Dolomie de Saint Dizier* Formation. F- Zoom on a silicified nodule, La Fontaine quarry, *Dolomie supérieure* Formation. Note the zoom location of the thin-section observation in H. G- Zoom of silicified nodules characterizing the LF4e Lithofacies, La Fontaine quarry, *Dolomie supérieure* Formation dolomicrite (LF4b). H- Observation of silica nodule in thin-section (LF10 thin section) showing cauliflower-texture or rosette texture (Qz), La Fontaine quarry, *Dolomie supérieure* Formation.

4.3.6. Quartz (Qz)

Quartz crystals are only observed within the *Dolomie supérieure* and *Dolomie de Saint-Dizier* Formations in facies association FA4 (Fig. 14), within infra-millimetric to pluri-centimetric silicified nodules (Fig. 10D, F). On thin-sections, quartz occurs in two distinct forms: (1) in infra-millimetric nodules with cauliflower-texture or rosette-texture (Figs. 10H and 15G), and (2) in inclusion-free idiomorphic drusy pyramidal quartz crystals of 200–500 μm and up to several millimeters (Figs. 10F and 15F, H). Pyramidal quartz crystals are observed in association with fluorite crystals, but the relative timing between the two phases is unclear (Fig. 15H). Residual rhombohedral dolomite can be observed as inclusions within quartz. Under cathodoluminescence the quartz is always non-luminescent (Fig. 15F–H).

4.3.7. Blocky calcite cement (Calcite 2 – Cal2)

Blocky calcite cements are mainly observed within the *Dolomie supérieure* Formation and within the *Dolomie de Saint-Dizier* Formation in facies association FA4 (Fig. 14). This consists of mosaics of coarse to very coarse (100 μm up to 3 mm) scalenohedral clear non-ferroan calcite crystals of low magnesium calcite, displaying a bright orange luminescence (Figs. 10H and 15E–H).

4.3.8. Iron oxi-hydroxides – Goethite (Gth)

Iron oxi-hydroxides consist of dark-red crystals (up to 200 μm) observed in inter-granular spaces between detrital quartz grains (Fig. 12E). Iron oxi-hydroxides consist mainly of goethite (Gth), located only in sandstone facies (Fig. 12F, facies association FA5).

4.4. Stable isotopes

The oxygen isotope composition of calcite from 57 carbonate samples (Table 2) ranges between −6.9‰ and 5.1‰ and carbon isotope composition ranges between −8.7‰ and 1.8‰ (Fig. 17 and Table 2).

Globally, the median $\delta^{18}O$ values of FA1, FA2, and FA3, respectively of −1.8‰, −1.9‰, and −1.3‰ (Fig. 17), are very similar, and compatible with potentially preserved marine values for this time period (Dera et al., 2011). The values for facies association FA4 are really distinct from the previous set and heavier overall, with a median at 3.6‰.

The median $\delta^{13}C$ values of facies associations FA1, FA2, FA3 and FA4 are respectively 1.2‰, −0.9‰, 0.5‰ and −0.8‰ (Fig. 17).

The oxygen isotope compositions of dolomite from 15 carbonate samples, composed by a mixture of calcite and dolomite (Table 2), range between −7‰ and 4.1‰ and carbon isotope compositions range between −5.8‰ and 2.1‰ (Fig. 17 and Table 2).

By their $\delta^{18}O$ and $\delta^{13}C$ signatures, four main distinct groups of samples can be deduced (Fig. 17). (1) Calcitic samples from facies association 1 ($n = 5$, upper offshore), from facies association 2 (9 of 20 samples, shoreface) and from facies association 3 (8 of 13 samples, shoreface) define the primary seawater signal with $\delta^{18}O$ ranging from −2‰ to 0‰ and $\delta^{13}C$ ranging from −1‰ to 2‰ (Fig. 17). (2) Calcitic samples from facies association 4 ($n = 19$, supratidal, brine ponds), with $\delta^{18}O$ ranging from 3‰ to 5‰ and $\delta^{13}C$ ranging from −1‰ to 2‰, define calcite that crystallized from brines (Fig. 17). (3) Dolomites from facies association 4 ($n = 8$, supratidal, brine ponds), with $\delta^{18}O$ ranging from 2‰ to 4‰ and $\delta^{13}C$ ranging from −1‰ to 2‰, define dolomite that crystallized from brines under evaporative conditions

Fig. 11. A- Outcrop of la Longue Queue quarry showing evaporite dissolution breccias or collapse breccias in the *Dolomie supérieure* Formation. The Jurassic Cretaceous Unconformity (JCU) is located between the *Dolomie supérieure* Formation and the Dolomie de Saint-Dizier. B- Zoom of collapse breccias and dissolution breccia in the *Dolomie supérieure* Formation in the la Longue Queue quarry. C- Tepee structure in microbially laminated calci-mudstone (LF4a) and associated dolomitic clays with silicified nodules of anhydrite precursor (Lithofacies LF4e) at the La Fontaine quarry, *Dolomie supérieure* Formation.
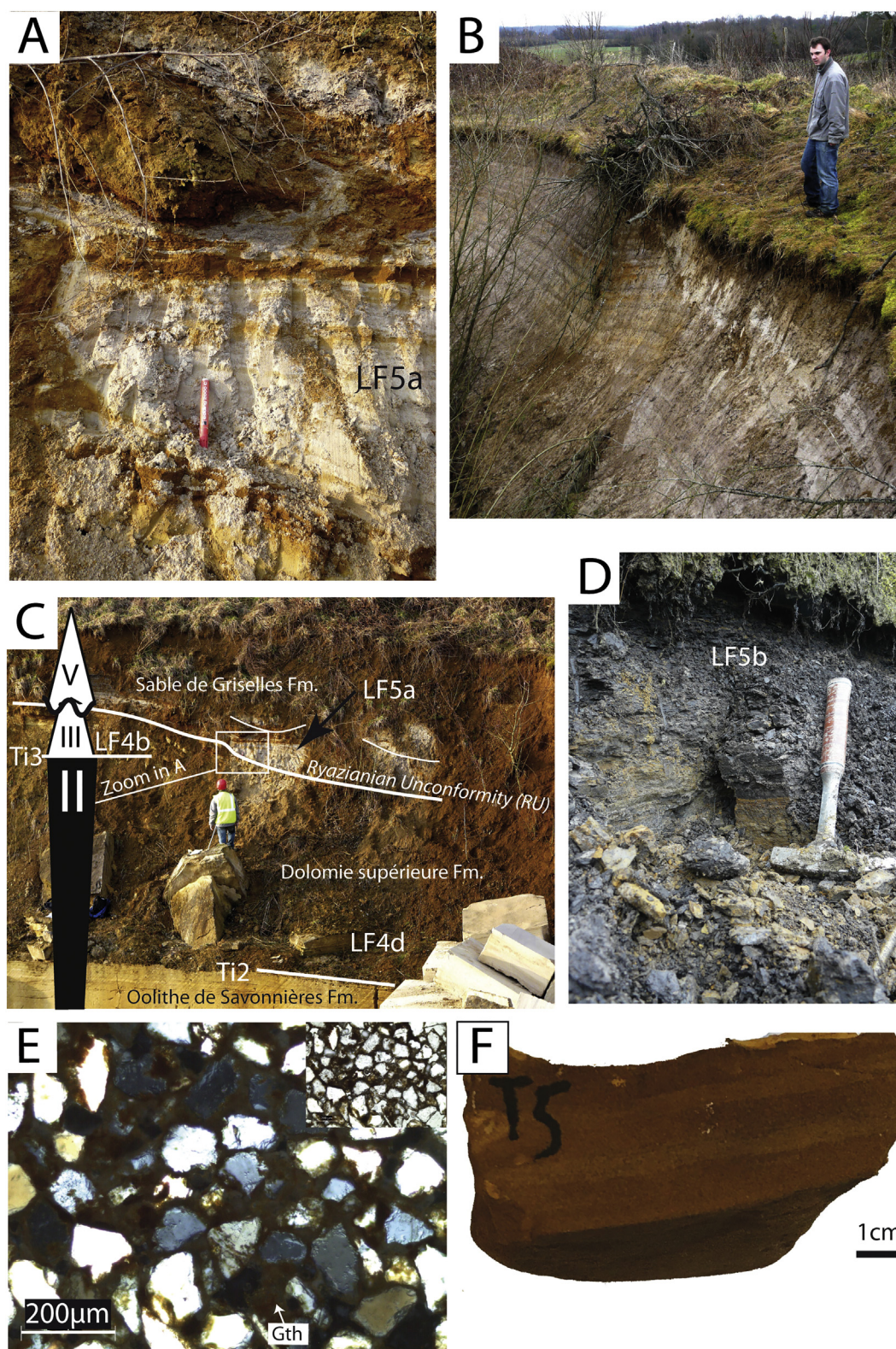
Fig. 12. A- Sand Lithofacies LF5a of the lower part of a channel in the Champ Maillot quarry, *Sable de Griselles* Formation. Zoom located in C. B- Outcrop of the Terme quarry showing the *Sable de Griselles* Formation. C- Stratigraphic succession in the Champ Maillot quarry showing the *Oolithe de Savonnières* Formation, the *Dolomie supérieure* and the *Sable de Griselles* Formation. The Ryazanian Unconformity is located at the base of the *Sable de Griselles* Formation. D- Organic rich silt layers (Lithofacies LF5b), Champ Maillot quarry. E- Sandstone lithofacies LF5a showing an intergranular goethite cement, sample T5, Terme quarry, *Sable de Griselles* Formation. F- Sandstone lithofacies LF5a sample T5, Terme quarry, *Sable de Griselles* Formation.

(Fig. 17). The 2 dolomitic samples from facies association 2 and the sample from facies association 3 in this domain suggest that evaporative conditions can succeed to marine conditions (Fig. 17). (4) Low $\delta^{18}O$

ranging from −4‰ to −6‰ and low $\delta^{13}C$ ranging from −6‰ to −9‰ of three samples clearly indicate a meteoric diagenesis impact (for facies associations 1, 2, and 3, Fig. 17). As meteoric fluids are $\delta^{18}O$ and $\delta^{13}C$

Fig. 13. Correlation diagram of the Tithonian, Berriasian, and early Valanginian in the eastern Paris Basin on a Poisson-Houpette transect. This illustration is composed of six outcrop sections studied in this work supplemented by previous descriptions of two outcrop sections (Rusciadelli, 1996) and 2 boreholes (http://infoterre.brgm.fr). Five 3-rd order sequences are recognized (I to IV) delimited by sequence boundaries.

Fig. 14. Paragenetic sequence of the Tithonian, Berriasian, and early Valanginian deposits in the eastern Paris Basin. The diagenetic stages are composed of: (1) isopachous fibrous cements (Calcite 0), (2) scalenohedral or rhombohedral calcite cement (Calcite 1), (3) dissolution of aragonite shells, of calcitic ooids and of anhydrite precursors, (4) dolomite (Dolomite 1 and 2), (5) fluorite, (6) quartz, and (7) blocky calcite (Calcite 2).

depleted, calcite crystallization under meteoric fluid causes decrease of $\delta^{18}O$ and $\delta^{13}C$. (4) Some samples from facies association 2 ($n = 3$, shoreface) and 4 ($n = 3$, supratidal, brine ponds) show $\delta^{13}C$ depletion caused by sub-surface organic matter alteration (Fig. 17). As organic matter is ^{12}C-rich, its alteration and oxidation in subsurface causes $\delta^{13}C$ depletion of groundwaters, and deplete $\delta^{13}C$ of subsequent calcite (Fig. 17).

4.5. Decompacted sedimentation, accommodation, subsidence, and tectonic subsidence

- *Sequence I (early Tithonian).* Sedimentary facies of the regressive systems tract of Sequence I record a bathymetric decrease of about 25 m, from 30 m to 5 m (Fig. 18, Table 3). About 60 m of decompacted sediments were deposited ($\approx$280 m/My) and an accommodation creation of about 30 m ($\approx$150 m/My) is calculated for this interval. A eustatic fall of 50 m from the beginning to the end of regressive systems tract of Sequence I is calculated (Haq, 2014). A subsidence of 80 m can be estimated ($\approx$400 m/My) and a tectonic subsidence of 60 m ($\approx$320 m/My) can be calculated (Fig. 18, Table 3).
- *Sequence II (early Tithonian).* The transgressive systems tract of this sequence is characterized by a decompacted sediment thickness of 16 m, and a 5 m increase in paleodepth, creating accommodation of about 20 m. A eustatic rise of 60 m is estimated (Haq, 2014), so a negative subsidence of −40 m (rate of −50 m/My) corresponding to an uplift is necessary to explain the 5 m increase in paleodepth during this eustatic rise (Fig. 18, Table 3). The regressive systems tract of Sequence II is marked by what corresponds to a decompacted sediment thickness of 6 m and a bathymetric fall of 15 m, at the origin of the exposure surface at the top of Sequence II. A negative accommodation of about −10 m is deduced (Fig. 18, Table 3). A sea-level fall of 40 m is proposed (Haq, 2018), giving a calculated subsidence of 30 m (subsidence rate of 20 m/My, Fig. 18, Table 3). The calculated tectonic subsidence is 40 m with a rate of 30 m/My (Fig. 18, Table 3).
- *Sequence III (early-late Tithonian).* The transgressive systems tract of this sequence is characterized by a decompacted sediment thickness of 6 m and very stable paleobathymetry. A 6 m accommodation creation can be deduced (Fig. 18, Table 3). Since a sea-level rise of 40 m is calculated during this period (Haq, 2014), an uplift of 30 m (rate of 40 m/My) is necessary to explain the stable paleodepth during this eustatic rise (Fig. 13). The calculated tectonic subsidence is of −60 m with a rate of 60 m/My. The regressive systems tract of Sequence III is characterized by a very low decompacted sediment thickness of

3 m, and by very stable paleodepth. In the La Fontaine section, accommodation is 3 m, and as a eustatic rise of 10 m occurred, an uplift of about +10 m is estimated (Fig. 18, Table 3). The 30 m-thick sediments corresponding to depositional Sequences II and III at La Fontaine are missing from the La Houpette and Poisson sections (Fig. 13). An erosional surface corresponding to a sedimentary *hiatus* has been described for the study area. The *hiatus* extends between the *Calcaire du Barrois* Formation (early Tithonian-Sequence I) and the *Sables de Griselles* (Valanginian-Sequence V) in the Poisson section, and between the *Calcaire du Barrois* Formation (early Tithonian-Sequence I) and the *Dolomie de Saint-Dizier* (early Berriasian - Sequence IV) in the La Houpette section. An elevation of +30 m can be deduced at the Poisson and La Houpette locations, and an accommodation of −30 m. At Poisson and La Houpette, the uplift can be estimated at about 40 m (Figs. 13 and 18, Table 3).

- *Sequence IV (early Berriasian).* The transgressive systems tract of Sequence IV is marked by a decompacted sediment thickness of 9 m and by a 15 m increase in paleodepth in the La Fontaine section, and 50 m in the Poisson section. This corresponds to the creation of accommodation of about 20 m in the La Fontaine section and 60 m in the Poisson section (40 m on average, Fig. 18, Table 3). A eustatic rise of 50 m is proposed (Haq, 2014), so uplifts of 30 m in the La Fontaine section and of 10 m in the La Houpette section are deduced, as well as a subsidence of about 10 m in the Poisson section (−10 m on average; mean rate of uplift 0 m/My, Fig. 18, Table 3). The regressive systems tract of Sequence IV is characterized by a decompacted sediment thickness of about 5 m (Fig. 18). An erosional surface corresponding to a *hiatus* of most of the upper Berriasian is observed in the study area. This erosional surface corresponds to the possible erosion of part or all of the depositional Sequence IV (18 m). The erosion reaches down to the *Dolomie inférieure* Formation in core 219-VT, where even Sequences II and III are eroded, which suggests that the elevation may have reached +30 m locally at the end of the early Berriasian (Figs. 13 and 18). Accommodation is about −20 m and a stable sea-level is estimated (Haq, 2014). A negative subsidence and tectonic subsidence corresponding to an uplift of 20 m can be calculated (Fig. 18, Table 3).
- *Sequence V (late Berriasian).* The transgressive systems tract of Sequence V is characterized by a decompacted sediment thickness of 6 m. Supratidal marsh in a fluvio-estuarine environment suggests a paleo-elevation of about +5 m. Accommodation is estimated at about 10 m. The late Berriasian is marked by an estimated eustatic rise of about 20 m (Haq, 2014), a negative subsidence of −10 m, with an uplift rate of 0 m/My (Fig. 18). A negative tectonic subsidence of −20 m/My is calculated (Fig. 18).
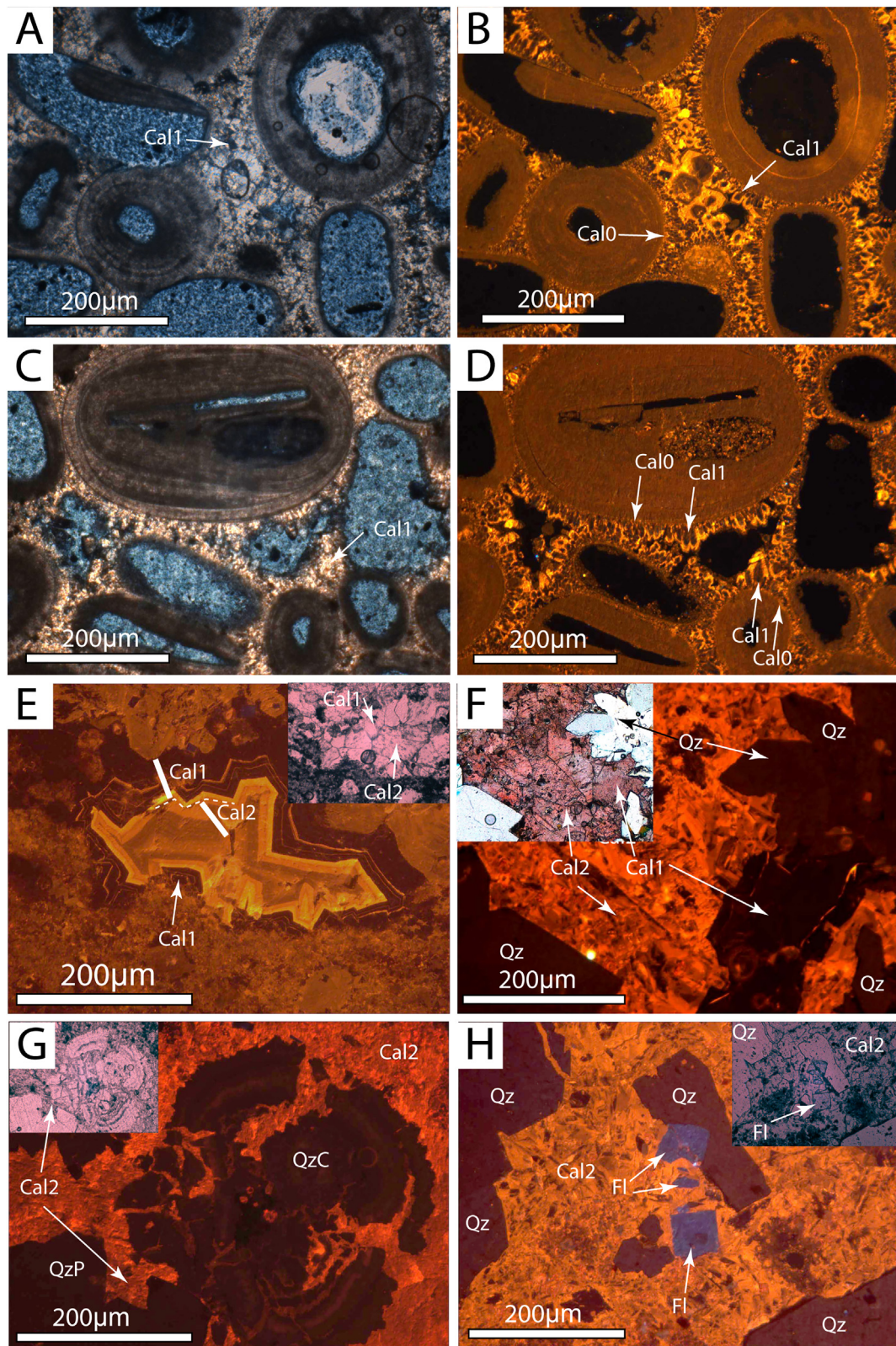
Fig. 15. A- Intergranular calcite cements Cal1 in Lithofacies LF2a, sample CHM7, Champ Maillot quarry, *Oolithe de Savonnières* Formation. B- Cathodoluminescence image of isopachous fibrous cement Cal0 and scalenohedral cement Cal1, sample CHM7, same view as A. C- Intergranular calcite cements Cal1 in Lithofacies LF2a, sample CHM7, Champ Maillot quarry, *Oolithe de Savonnières* Formation. D- Cathodoluminescence image of isopachous fibrous cement Cal0 and scalenohedral cement Cal1, sample CHM7, same view as C. E- Cathodoluminescence image of rhombohedral cement Cal1 and blocky calcite Cal2 in the dolomitic muds with silicified nodules of anhydrite precursor (Lithofacies LF4e), La Fontaine quarry, sample LF9, *Dolomie supérieure* Formation. F- Cathodoluminescence image of idiomorphic drusy pyramidal quartz crystals (Qz) and Calcite 1 and 2 (Cal1 and Cal2) in the dolomitic muds with silicified nodules (Lithofacies LF4e), La Fontaine quarry, sample LF9, *Dolomie supérieure* Formation. G- Cathodoluminescence image of silica nodules with cauliflower-texture (QzC) and pyramidal quartz crystals (QzP), La Fontaine quarry, sample LF10, *Dolomie supérieure* Formation. H- Cathodoluminescence image of cubes of fluorite (Fl), idiomorphic drusy pyramidal quartz crystals (Qz) and blocky calcite cement (Cal2) in the dolomitic muds with silicified nodules of anhydrite precursor (Lithofacies LF4e), La Fontaine quarry, sample LF10, *Dolomie supérieure* Formation.
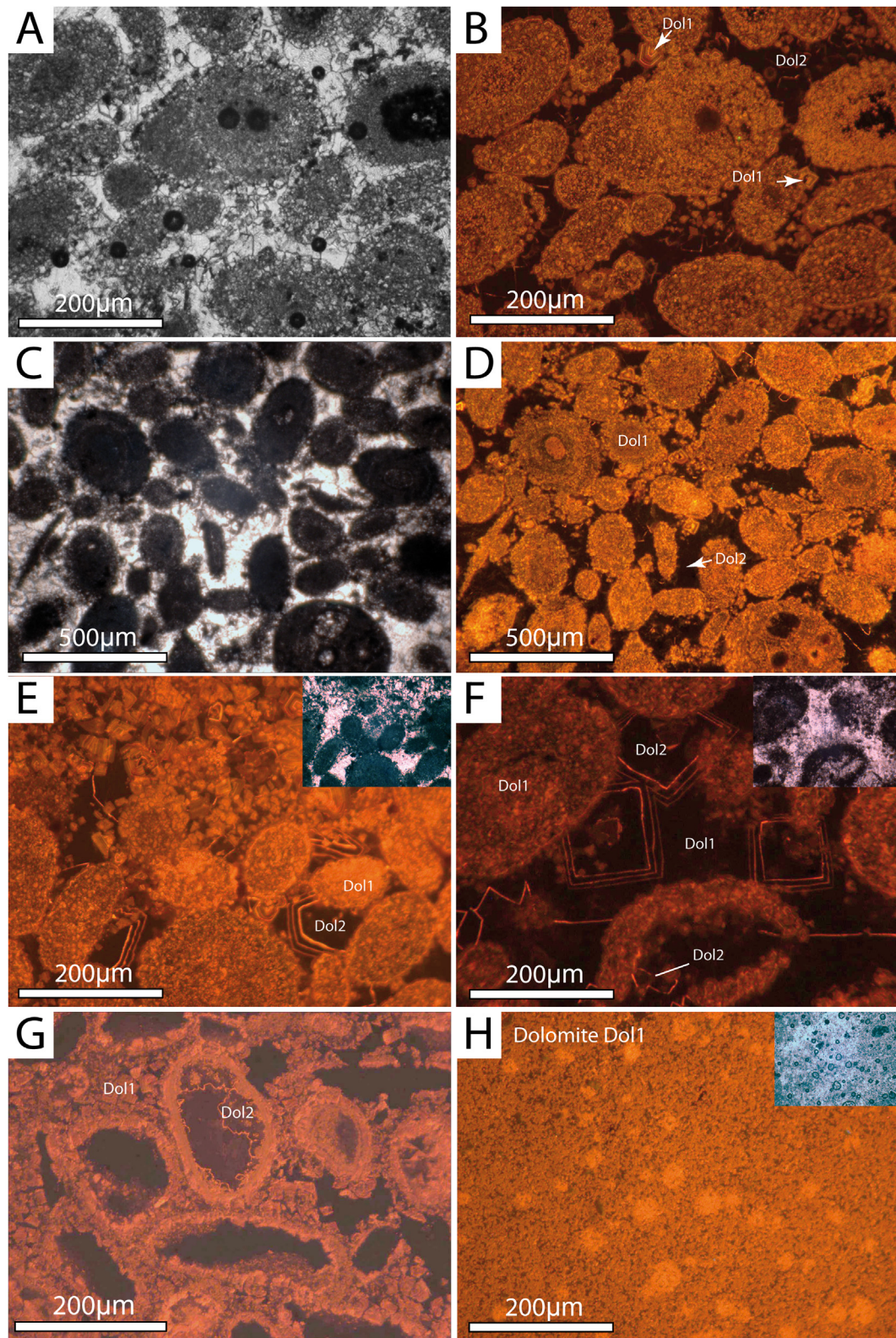
Fig. 16. A- Dolomitization process of ooid grainstone (Lithofacies LF2a) in the *Dolomie de Saint Dizier* Formation, sample LF12, La Fontaine quarry. B- Cathodoluminescence image of dolomitization process Dolomite 1 and 2, sample LF12, La Fontaine quarry, *Dolomie de Saint Dizier* Formation. Same view as A. C- Dolomitization process of ooid grainstone (Lithofacies LF2a) in the *Dolomie de Saint Dizier* Formation, sample LF12, La Fontaine quarry. D- Cathodoluminescence image of dolomitization process Dolomite 1 and 2, sample LF12, La Fontaine quarry, *Dolomie de Saint Dizier* Formation. Same view as C. E- Cathodoluminescence image of dolomitization process Dolomite 1 and 2, sample LF12, La Fontaine quarry, *Dolomie de Saint Dizier* Formation. F- Cathodoluminescence image of dolomitization process Dolomite 1 and 2, sample LF12, La Fontaine quarry, *Dolomie de Saint Dizier* Formation. G- Cathodoluminescence image of dolomitization process Dolomite 1 (Dol1) in intergranular space and Dol2 replacing calcitic ooids, sample T2, Terme quarry, *Oolithe de Savonnières* Formation. H- Cathodoluminescence image of dolomicrite Lithofacies LF4b with fine-grained crystals (<10 μm), sample CHM9, Champ-Maillot quarry, *Dolomie supérieure* Formation.

Table 2
Sample, outcrop, formation name, depth (m), texture and facies association, and associated δ¹⁸O and δ¹³C values of calcite and dolomite.

| Sample	Outcrop	Formation name	Depth (m)	Texture	Facies	Facies association	δ^{18}O PDB (Calcite)	δ^{13}C PDB (Calcite)	δ^{18}O PDB (Dolomite)	δ^{13}C PDB (Dolomite)
CHM7	Champs Maillot	Oolithe de Savonnières	0,8	Grainstone	LF2a	FA2	−1,9	−0,3		
CHM8	Champs Maillot	Oolithe de Savonnières	1,8	Grainstone	LF2a	FA2	−1,0	−0,5		
CHM8′	Champs Maillot	Dolomie supérieure	2,0	Calci-mudstone	LF4a	FA4	−0,1	−2,1		
CHM9-1	Champs Maillot	Dolomie supérieure	4,2	Dolomitic clayey facies	LF4d	FA4	3,9	−1,1		
CHM9-2	Champs Maillot	Dolomie supérieure	4,2	Dolomitic clayey facies	LF4d	FA4	3,4	−1,3	3,4	−1,1
CHM12-1	Champs Maillot	Dolomie supérieure	5,3	Dolostone	LF4c	FA4	5,1	0,5		
CHM12-2	Champs Maillot	Dolomie supérieure	5,3	Dolostone	LF4c	FA4	4,1	0,4	3,5	0,4
G1	Givrauval	Calcaires du Barrois	1,1	Grainstone	LF2b	FA2	−1,6	1,2		
G2	Givrauval	Calcaires du Barrois	3,8	Calci-mudstone	LF1a	FA1	−1,6	0,7		
G3	Givrauval	Calcaires du Barrois	8,4	Calci-mudstone	LF1a	FA1	−2,4	0,0		
LF1	La Fontaine	Oolithe de Savonnières	0,3	Grainstone	LF2a	FA2	−2,0	−0,1		
LF2	La Fontaine	Oolithe de Savonnières	1,0	Grainstone	LF2a	FA2	−2,3	−0,1		
LF3	La Fontaine	Oolithe de Savonnières	1,3	Grainstone	LF2a	FA2	−2,0	0,1		
LF4	La Fontaine	Oolithe de Savonnières	1,8	Grainstone	LF2a	FA2	−1,8	0,1		
LF5-bas	La Fontaine	Oolithe de Savonnières	1,9	Packstone	LF2a	FA2	−1,5	0,0		
LF5-H-1	La Fontaine	Oolithe de Savonnières	2,0	Calci-mudstone	LF3b	FA3	−1,8	−2,4		
LF5-H-2	La Fontaine	Oolithe de Savonnières	2,0	Calci-mudstone	LF3b	FA3	−2,5	−2,9	−2,9	−2,6
LF8	La Fontaine	Dolomie supérieure	3,4	Wackestone	LF4a	FA4	−6,1	−0,8		
LF11-1	La Fontaine	Dolomie de Saint-Dizier	6,9	Dolostone	LF4c	FA4	3,7	−0,6		
LF11-2	La Fontaine	Dolomie de Saint-Dizier	6,9	Dolostone	LF4c	FA4	2,9	−0,4	3,0	0,5
LF12-1	La Fontaine	Dolomie de Saint-Dizier	9,8	Grainstone	LF2a	FA2	−0,9	−3,5		
LF12-2	La Fontaine	Dolomie de Saint-Dizier	9,8	Grainstone	LF2a	FA2	−3,6	−4,7	2,9	0,9
LF13	La Fontaine	Dolomie de Saint-Dizier	10,7	Grainstone	LF2a	FA2	−3,9	−4,2	−7,0	−5,8
LF14	La Fontaine	Dolomie de Saint-Dizier	11,0	Grainstone	LF2a	FA2	−2,5	−1,5		
LQ15	Longue Queue	Oolithe de Savonnières	1,3	Grainstone	LF2a	FA2	−1,8	−1,3		
LQ17	Longue Queue	Oolithe de Savonnières	2,6	Grainstone	LF2a	FA2	−3,5	−0,6		
LQ18-1	Longue Queue	Oolithe de Savonnières	3,0	Packstone	LF3a	FA3	−1,3	−0,2		
LQ18-2	Longue Queue	Oolithe de Savonnières	3,0	Wackestone	LF3a	FA3	−0,6	−1,6		
LQ2-1	Longue Queue	Dolomie supérieure	3,9	Dolostone	LF4c	FA4	0,8	−3,1		
LQ2-2	Longue Queue	Dolomie supérieure	3,9	Dolostone	LF4c	FA4	1,3	−2,2	3,3	0,5
LQ8-1	Longue Queue	Dolomie de Saint-Dizier	9,3	Dolomicrite	LF4b	FA4	4,2	−0,5		
LQ8-2	Longue Queue	Dolomie de Saint-Dizier	9,3	Dolomicrite	LF4b	FA4	3,3	−0,8	2,7	−0,6
LQ9-1	Longue Queue	Dolomie de Saint-Dizier	9,4	Dolomicrite	LF4b	FA4	4,3	−1,2		
LQ9-2	Longue Queue	Dolomie de Saint-Dizier	9,4	Dolomicrite	LF4b	FA4	3,2	−1,3	4,1	−0,5
LQ11-1	Longue Queue	Dolomie de Saint-Dizier	10,4	Dolostone	LF4c	FA4	4,3	0,6		
LQ11-2	Longue Queue	Dolomie de Saint-Dizier	10,4	Dolostone	LF4c	FA4	3,6	0,6	2,9	0,8
LQ13-1	Longue Queue	Dolomie de Saint-Dizier	11,6	Grainstone	LF2a	FA2	1,0	−4,9		
LQ13-2	Longue Queue	Dolomie de Saint-Dizier	11,6	Grainstone	LF2a	FA2	1,3	−4,6	3,7	−0,8
M-1-1	Magneux	Calcaires du Barrois	20,1	Calci-mudstone to wackestone	LF3b	FA3	2,7	1,8		
M-1-2	Magneux	Calcaires du Barrois	20,1	Calci-mudstone	LF3b	FA3	−0,8	1,4	3,4	2,1
M1-1	Magneux	Calcaires du Barrois	23,6	Packstone	LF3a	FA3	−1,2	1,1		
M1-2	Magneux	Calcaires du Barrois	23,6	Packstone	LF3a	FA3	−1,2	1,1	−6,4	−3,2
M-4	Magneux	Calcaires du Barrois	25,6	Calci-mudstone	LF3b	FA3	−0,2	0,5		
M3	Magneux	Calcaires du Barrois	26,9	Calci-mudstone	LF3b	FA3	−4,2	−7,1		
M5	Magneux	Dolomie de Saint-Dizier	30,1	Calci-mudstone	LF4b	FA4	−6,9	−3,6		
M7	Magneux	Dolomie de Saint-Dizier	32,8	Grainstone	LF2c	FA2	−4,7	−8,7		
P6	Poissons	Calcaires du Barrois	0,1	Calci-mudstone	LF1a	FA1	−1,1	1,4		
P2	Poissons	Calcaires du Barrois	1,5	Calci-mudstone	LF1a	FA1	−2,0	1,2		
P3	Poissons	Calcaires du Barrois	2,6	Calci-mudstone	LF1a	FA1	−1,8	1,7		
P4	Poissons	Calcaires du Barrois	3,2	Wackestone	LF3b	FA3	−1,7	1,7		
P5	Poissons	Calcaires du Barrois	3,7	Calci-mudstone	LF3b	FA3	−2,4	1,5		
P11	Poissons	Calcaires du Barrois	4,0	Calci-mudstone to wackestone	LF3b	FA3	−5,3	−7,3		
T1	Terme	Oolithe de Savonnières	0,5	Grainstone	LF2c	FA2	−2,0	−0,4		
T2-1	Terme	Oolithe de Savonnières	2,8	Grainstone	LF2c	FA2	−0,8	−1,9		
T2-2	Terme	Oolithe de Savonnières	2,8	Grainstone	LF2c	FA2	−2,5	−3,0	1,5	−0,6
T3-1	Terme	Dolomie supérieure	3,9	Dolomicrite	LF4b	FA4	4,1	0,9		
T3-2	Terme	Dolomie supérieure	3,9	Dolomicrite	LF4b	FA4	3,6	0,7	3,5	0,5

5. Discussion

5.1. Quality of age model and correlation with the eustatic chart of Haq (2014, 2018)

Uncertainties in accommodation, subsidence, and tectonic subsidence calculation may be due to uncertainties in the estimates of (1) the eustatic variations by Haq (2014, 2018) for subsidence and tectonic subsidence calculations only, (2) the age model of the sections, (3) the decompacted sediment thickness, (4) paleodepth estimation from facies observations and characterizations. Overestimations of the amplitude of eustatic variations are the main criticisms of Haq's curves which could be a major bias in estimates of subsidence amplitudes

(Rowley, 2013; Andrieu et al., 2016). Although there is debate about this eustasy curve (Miller et al., 2005), it is the only curve precise enough to estimate eustatic variations at the time resolution used in this study, and so the only curve that can be used to reconstruct subsidence variations at the third-order sequence scale (Andrieu et al., 2016). Recent reappraisals of the Jurassic and Cretaceous sea-level history have been published (Haq, 2014, 2018). Always Eurocentric, the updated curve for the Jurassic/Cretaceous transition is extended to some parts of the Tethys toward the East (Haq, 2018). Precise amplitudes of drawdowns are often difficult to establish, 3rd order fluctuations are marked by base-level falls from 40 to 100 m (Figs. 2 and 18). Purbeck beds and Wealden facies age models of the eastern Paris Basin sections are the main uncertainty on the calculation of
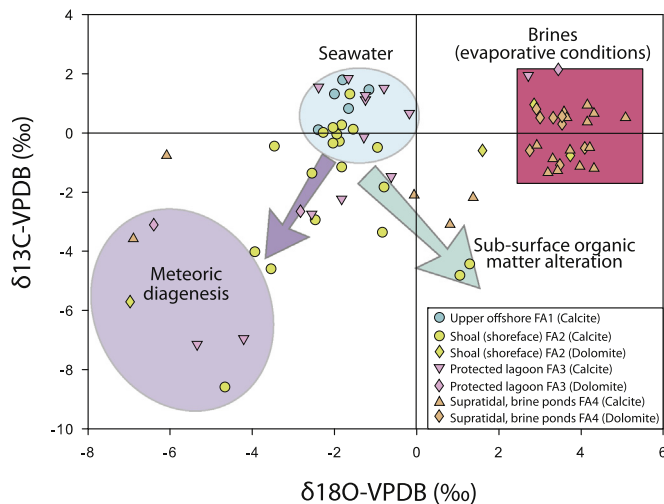
Fig. 17. $\delta^{18}O$ and $\delta^{13}C$ (‰-PDB) cross-plot with the different facies associations. Data from Champs Maillot, Givrauval, La Fontaine, Longue Queue, Magneux, Poissons and Terme quarries.

accommodation, subsidence, and tectonic subsidence curves. As no ammonites are found in eastern Paris Basin Purbeck beds and Wealden facies, the biostratigraphic determinations are only made using organic-walled cysts of dinoflagellates (Buissart et al., 1988; Rusciadelli, 1996). Dinocysts form important correlation tool for the North Sea and Paris Basin, where their datums are correlated to ammonite zones of the Boreal realms (e.g., Gradstein et al., 2012). Faunal provincialism of ammonites in Jurassic/Cretaceous transition times and the use of different zonal schemes based on ammonites and dinoflagellate cysts affect the precision in biostratigraphic age determination, and so correlation with the eustatic curve of Haq (2014, 2018). Calculated values are rounded to the nearest 10 m and amplitude of variation must be used with precautions, but trends of subsidence *versus* uplift could be interesting data to discuss. The uplift trend from Tithonian to Valanginian has to be taken into consideration and demonstrates that the Jurassic/Cretaceous transition is subject to important geodynamic re-organization at the lithosphere scale.

5.2. From the Jurassic carbonate platform to Wealden facies in western European Basins

The detailed Tithonian and Berriasian sedimentary facies analysis allows us to highlight two distinct depositional models for the studied interval, i.e. (1) a carbonate ramp model, and (2) and an upper deltaic plain model (Fig. 19A–B). The first depositional model is applicable from the early Tithonian to the early Berriasian (Figs. 19A and 20A–C). The carbonate platform comprises four main depositional environments with, from distal to the more proximal: (1) upper offshore, (2) shoreface, (3) lagoon, and (4) supratidal marshes or brackish ponds (Fig. 19A). The deposits of the beginning of the Tithonian (Sequences I, II, and III) correspond to marine limestone laid down in an offshore setting, dolomitic clays, and evaporites deposited in a supratidal setting (Fig. 20A). The *Oolithe de Savonnières* limestone bounded by the *Dolomie inférieure* and *Dolomie supérieure*, form the "Purbeckian" facies, well expressed in the Anglo-Paris Basin at this time (Jacquin et al., 1998b), capped in the study area by the JCU (Fig. 20B). Carbonate sedimentation resumed in the earliest Berriasian (*Lamplughi* Zone) but for a short period, ending at the end of the early Berriasian (*Runctoni* Zone, Fig. 20C). The second large sedimentary hiatus is the RU (Fig. 20D), corresponding to the maximum regression between the second-order cycles 10 and 11 *sensu* Jacquin et al. (1998a, 1998b). This unconformity is associated with significant differential erosion in the study area (Fig. 20D).

The second depositional model is applicable from the latest Berriasian and corresponds to an upper deltaic plain model dominated by fluvial environmental processes (Figs. 19B and 20D). Distributary channels in similar systems migrated over much of the Anglo-Paris Basin and gave rise to the Wealden facies (Allen, 1959; Mégnien and Mégnien, 1980; Rusciadelli, 1996; Jacquin and de Graciansky, 1998a; Jacquin et al., 1998b). The Wealden facies were deposited from the early Berriasian onward, and clastic sedimentation continued up until the Albian in the Paris Basin (Fig. 20D, Mégnien and Mégnien, 1980, Buissart et al., 1988). The onset of the Wealden facies, marked by delta plain environments, is well-dated by dinocysts of the *Stenomphalus* Zone (late Berriasian) in the Paris Basin within the *Sables de Griselles* Formation (France; Rusciadelli, 1996; Jacquin et al., 1998b), by dinocysts or ostracods of the *Stenomphalus* Zone (late Berriasian) in the Weald and Wessex Basins (UK; Allen and Wimbledon, 1991; Hesselbo and Allen, 1991; Jacquin et al., 1998b), and by dinocysts and ostracods of the *Kochi* Zone (mid Berriasian) in the Lower Saxony Basin within the *Buckeburg* Formation (Fig. 3; Germany and Netherlands, Strauss et al., 1993).

The sudden complete demise of Jurassic carbonate platform sedimentation in the Paris Basin, occurred just after the early Berriasian (Mégnien and Mégnien, 1980; Rusciadelli, 1996; Jacquin et al., 1998a; Jacquin et al., 1998b). This major environmental change is well expressed throughout West European basins (Allen and Wimbledon, 1991; Hesselbo and Allen, 1991; Jacquin et al., 1998a; Jacquin and de Graciansky, 1998a; Jacquin et al., 1998b).

5.3. Climatic and geodynamic control on carbonate platform development and demise

From the Tithonian to the early Berriasian, Sequences I, II, III, and IV record carbonate platform sedimentation. Sequences I, II, and III identified in this study do not integrate well with the previously published (Hardenbol et al., 1998) sequence stratigraphic interpretations at the scale of the north–west Tethyan domain (Fig. 3), whereas Sequence IV is more in accordance with interpretations by Hardenbol et al. (1998).

The second-order transgressive/regressive (T/R) cycles T/R 9 and T/R 10 *sensu* Jacquin et al. (1998a, 1998b) are synchronous over western European basins, even though extensional tectonics were particularly active at that time, which suggests a tectono-eustatic control (Jacquin and de Graciansky, 1998b). Consequently, deposition of Sequence IV was probably driven by a tectono-eustatic control. The three previous sequences I to III were more influenced by local variations in subsidence/uplift and variable rates (Jacquin and de Graciansky, 1998b). The transition from Sequence I to Sequence II corresponds to an abrupt change from high accommodation rate (~150 m/My) and subsidence rate (~400 m/My, Fig. 21) to low accommodation rate (~20 m/My) and an uplift of ~50 m/My (Fig. 21). The transition from Sequence II to Sequence III corresponds also to an abrupt change from a subsidence of ~20 m/My to an uplift regime of ~40 m/My (Fig. 21). The transition from Sequence III to IV is marked by a sedimentary gap of a part of the late Tithonian, with no sedimentary record in the eastern part of the Paris Basin (Figs. 18 and 21). Sequence stratigraphic correlations and associated interpreted sedimentary architectures show that the JCU is an important local structural episode characterized by the creation of a regional scale basin through a tectonic flexural deformation (Fig. 20B). A NW–SE to W–E flexure of approximately 15 km-wide and 30 km-long (Figs. 1 and 20B) formed during the development of the JCU. Stratigraphic reconstructions suggest that vertical deformation could be of about 5–10 m, corresponding to sedimentary thickness between JCU and RU (Fig. 13). In the Paris Basin, NE to SW compression caused uplifts along the eastern border of the Armorican Massif, the Poitou High, and the southern border of the London Brabant Massif, and also induced a NW–SE medium wavelength flexure of Jurassic deposits in northern France (Guillocheau et al., 2000). These flexural events at a very local scale or at regional scale are interpreted as a consequence of
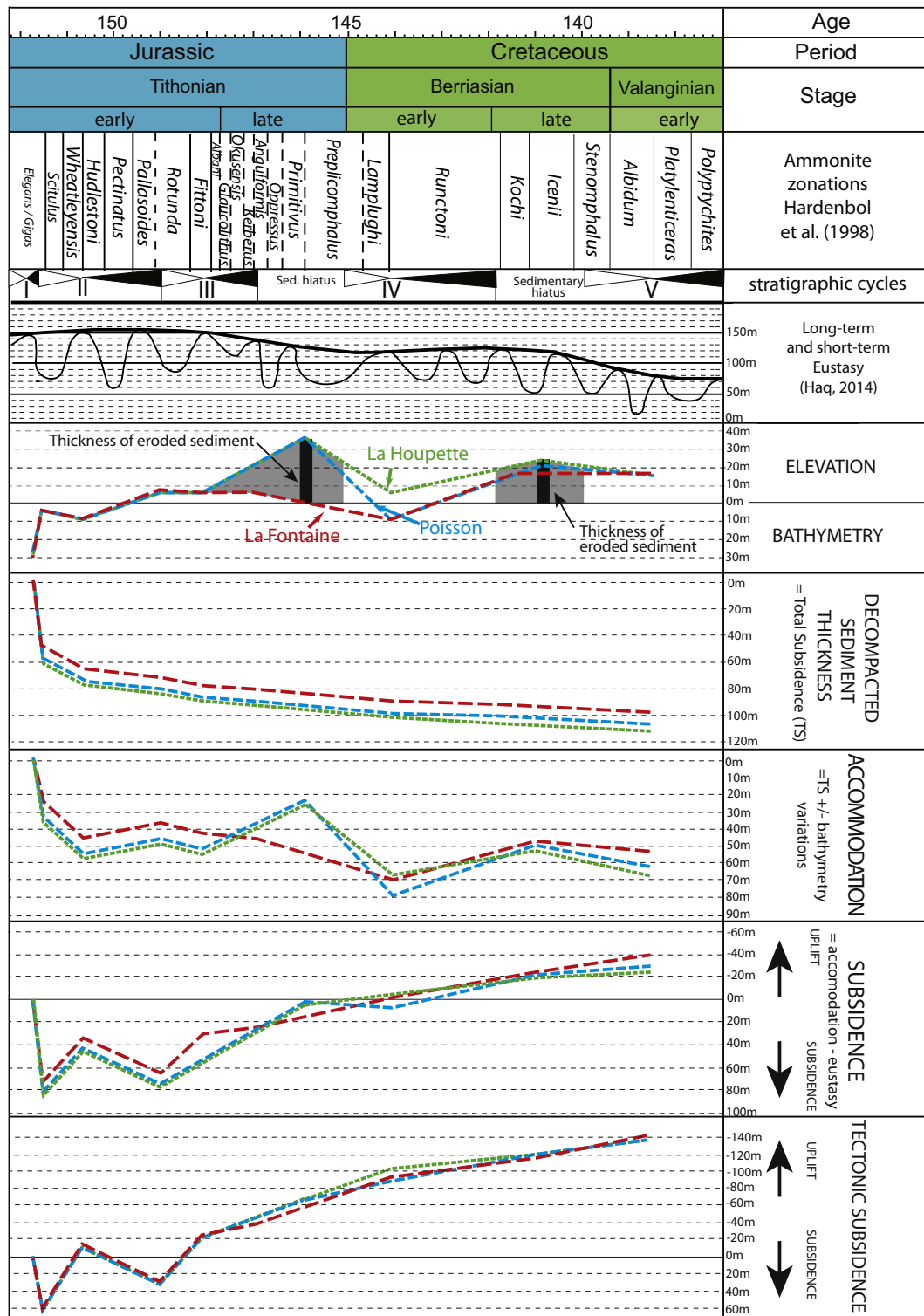
Fig. 18. Chronostratigraphic diagram showing eastern Paris Basin sequences, eustasy curve (Haq, 2014), bathymetry, decompacted sediment thickness, accommodation, subsidence, and tectonic subsidence curves in the eastern Paris Basin at La Fontaine, La Houpette, and Poisson.

the extensional tectonics in southern and northern Europe, related to the opening of the central Atlantic Ocean and North Sea (Ziegler, 1988; Jacquin and de Graciansky, 1998a). This geodynamic context at the Jurassic/Cretaceous boundary was favorable to numerous earthquakes, potentially responsible for tsunamis, one of them being recognized from deposits in the Purbeck beds of the Boulonnais area (France; Deconinck et al., 2000; Schnyder et al., 2005a). After this active geodynamic period, or set of events, carbonate sedimentation resumed

with the deposition of supratidal dolomitic facies in the study area, meaning that the JCU may only be considered as the onset of the demise of the carbonate platform in the Paris Basin, but not the only cause of it.

Riboulleau et al. (1998) reconstruct the evolution of the paleotemperatures of the Russian Platform over the Late Jurassic with $\delta^{18}O$ on belemnite rostra. Oxygen isotope compositions indicate an intense warming trend from the Oxfordian (7 °C) to the Kimmeridgian (18 °C), temperatures were stable over the Kimmeridgian and Volgian

Table 3
Eustatic variations, bathymetry, decompacted sediment thickness, accommodation, subsidence, and tectonic subsidence in the eastern Paris Basin at La Fontaine, La Houpette, and Poisson.

	Sequence	Sequence I RST	Sequence II TST	Sequence II RST	Sequence III TST	Sequence III RST	Sequence IV TST	Sequence IV RST	Sequence V TST
	Eustasy (m)	−50	60	−40	40	10	50	0	20
	Duration (My)	0,20	0,85	1,65	0,90	1,15	2,90	2,25	3,25
Bathymetric variation (m)	*Poissons*	−25	5	−15	0	−30	50	−30	10
	La Fontaine	−25	5	−15	0	0	20	−30	0
	La Houpette	−25	5	−15	0	−30	30	−20	10
Decompacted sediment thickness (m)	*Poissons*	58	16	6	6	3	9	2	6
	La Fontaine	49	16	6	6	3	9	2	6
	La Houpette	61	16	6	6	3	9	5	6
	Mean	60	20	10	10	0	10	0	10
	Rate (m/My)	280	20	0	10	0	0	0	0
Accommodation	*Poissons*	30	20	−10	10	−30	60	−30	10
	La Fontaine	20	20	−10	10	0	20	−20	10
	La Houpette	40	20	−10	10	−30	40	−10	10
	Mean	30	20	−10	10	−20	40	−20	10
	Rate (m/My)	150	20	−10	10	−20	10	−10	0
Subsidence (accommodation - eustasy)	*Poissons*	80	−40	30	−30	−40	10	−30	−10
	La Fontaine	70	−40	30	−30	−10	−30	−20	−10
	La Houpette	90	−40	30	−30	−40	−10	−10	−10
	Mean	80	−40	30	−30	−30	−10	−20	−10
	Rate (m/My)	400	−50	20	−40	−20	0	−10	0
Tectonic subsidence	*Poissons*	60	−70	40	−60	−40	−20	−30	−20
	La Fontaine	60	−70	40	−60	−10	−50	−20	−30
	La Houpette	70	−70	40	−60	−40	−40	−20	−20
	Mean	60	−70	40	−60	−30	−40	−20	−20
	Rate (m/My)	320	−90	30	−60	−30	−10	−10	−10

(Riboulleau et al., 1998). This warming trend is also observed in the Paris Basin from the late Oxfordian (16 °C) to Kimmeridgian (26 °C, Brigaud et al., 2008). On the other hand, temperatures from oxygen measurements on belemnites or bivalves are much rarer for the Tithonian and paleoclimatic reconstructions for this period are perfectible, and should be taken with precautions (Dera et al., 2011). Palynomorph assemblages from the southern North Sea recorded a warming phase in the *Wheatleyensis* and *Hudlestoni* zones of the early Tithonian, warm conditions extending up to the end of the early Berriasian *Runctoni* zone (Fig. 21, Abbink et al., 2001). Martinez and Dera (2015) confirmed a relatively warm interval in the North-West Tethyan domain during the Tithonian, ending at the end of the Tithonian. The early Tithonian warming is coupled with aridification suggested by palynomorph assemblages that extend to the early late Berriasian (*Kochi* zone, Abbink et al., 2001). Clay mineral assemblages (absence of kaolinite) or organic-matter distribution also suggest semi-arid conditions during the late Tithonian-early Berriasian interval on the scale of the western Tethyan domain (Deconinck, 1987; Deconinck, 1993; Ruffell and Rawson, 1994; Allen, 1998; Ramail, 2005; Schnyder et al., 2005b; Schnyder et al., 2006; Schnyder et al., 2009). This warming and aridification coincided in the study area with the transition from oolithic limestone to restricted dolomitic deposits. The early Tithonian was a period marked by low $\delta^{13}C$ composition in NW Tethys (Fig. 21, Martinez and Dera, 2015). Oxidation of algal ^{12}C deposits and terrestrial organic carbon from fluvial discharges prevented carbon burial, released ^{12}C to seawater and lead to consequent decrease of $\delta^{13}C$ values in the oceanic reservoir, explaining the decrease of $\delta^{13}C$ values measured on belemnites (Martinez and Dera, 2015). The early Tithonian was a period of high eccentricity with ^{12}C-enriched seawater, with typically high seasonal contrasts, and high carbonate production rates, owing to large carbonate influxes and supersaturation under evaporating conditions (Martinez and Dera, 2015; Andrieu et al., 2016). In a nutshell, climatic conditions were still favorable for carbonate production at least up to the end of the early Tithonian, *i.e.* before the JCU.

But these semi-arid and warm conditions together with (1) the overall second-order regressive trend during Sequences II and III, and (2) the flexural deformation linked to the JCU, which probably increased the restriction of depositional environments, easily explain the intense

dolomitization that affected the lower Tithonian sediments in the study area. The fine crystalline aspect of the replacive dolomite (Dol1), the stratiform nature of dolomite bodies, the occurrence with silica pseudomorphs of evaporites, and the solution-collapse breccias are evidence of early dolomitization within the Purbeckian facies, either through a stable sabkha-like process, with steady state depositional conditions, or through brine-reflux processes (Warren, 2000). The absence of large scale preserved evaporite deposits, or of evidence of their existence such as very large scale collapse breccias, preferentially supports sabkha-like processes. In any case, the positive $\delta^{18}O$ values (from 0‰ to +4‰) of calcite analyzed in these dolomitized levels and of dolomites definitely illustrate evaporative conditions (Warren, 2000). The $\delta^{18}O$ and $\delta^{13}C$ isotopic compositions of dolomites compare very well with Holocene dolomites from Abu Dhabi originated from brines in evaporitic sabkha environment (Warren, 2000). It is noteworthy that the ooid grainstone facies defining the MFS of Sequence II (*Oolithe de Savonnières* Formation) are extremely weakly dolomitized in the studied outcrops, although they can be totally dolomitized in other locations (Lorenz and Lehrberger, 2013). This is probably due to the heterogeneity of the intensity of the early cementation filling the interparticle pore-space (fibrous cements and faint dogtooth cements, Figs. 8A, 14), which locally prevented the flow of dolomitizing fluids. The isotopic compositions in dolomitized ooid grainstone facies suggest that brine fluids influx into marine carbonates and indicate that evaporative conditions in supratidal and brine pond environments can succeed to marine conditions.

The RU marks a more critical change in the study area with the transgressive clastics of the late Berriasian and early Valanginian Wealden facies, unconformably overlying the "Purbeckian" and the Tithonian limestones, and even other lower Upper Jurassic strata down to the Oxfordian (Fizaine, 2012). This RU is more widely found in the Netherlands, where Valanginian clastic reservoirs directly cover a Zechstein or Triassic paleorelief (Cottençon et al., 1975). Over the western Tethyan domain, carbonate platforms were subject to karstification in the Jura, Moesia, and Apulia (Jacquin and de Graciansky, 1998a).

The abrupt stoppage of carbonate production at the end of the early Berriasian in the Paris Basin (Mégnien and Mégnien, 1980; Rusciadelli, 1996; Jacquin et al., 1998b), occurred after or during the establishment

A- From Middle Tithonian to Early Berriasian - Carbonate platform
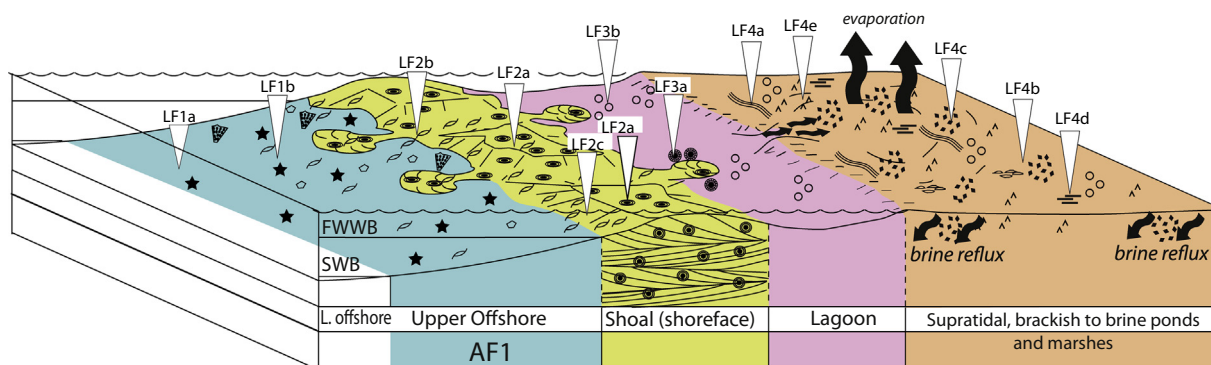
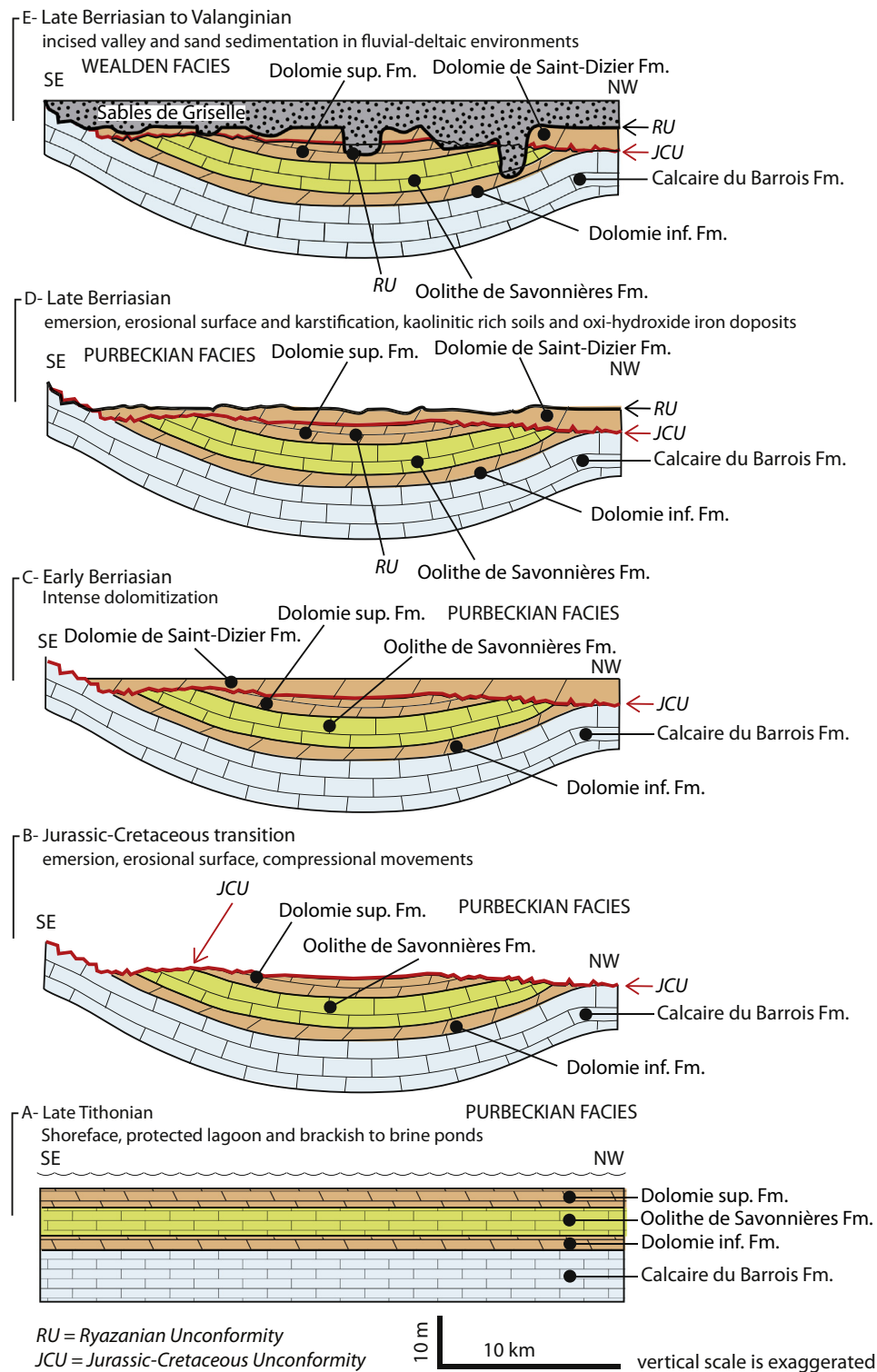## B- From Late Berriasian to Valanginian - Delta plain environment
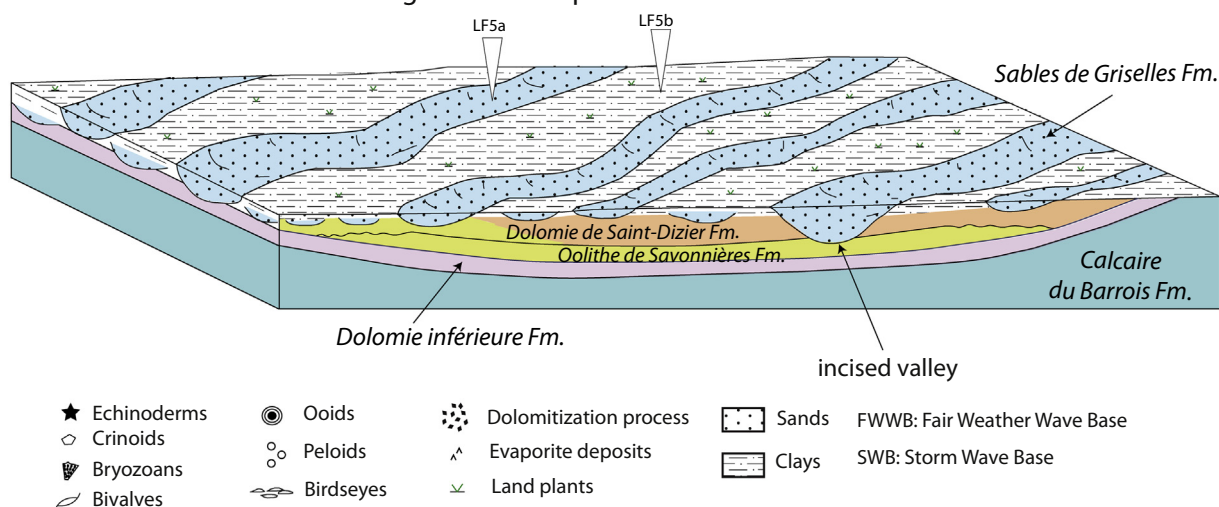
Fig. 19. Changing depositional environment from the Tithonian to Valanginian in the eastern Paris Basin with lithofacies distribution. A- Carbonate platform with a supratidal area leading to dolomitization. B- Delta plain environment with distributary-channel migration and incision associated with fluvial sedimentation processes.

of a relatively cool climate initiated either from the latest Tithonian or the early Berriasian in the western Tethys domain depending on the references (Abbink et al., 2001; Grabowski et al., 2013; Martinez and Dera, 2015). At high latitudes, the first occurrence of glendonites during the late Berriasian in the northern hemisphere confirms a significant climate change (Rogov et al., 2017). This cooling is associated with a very fast change from semi-arid to humid conditions in the late Berriasian *Icenii* Zone (Fig. 22; Abbink et al., 2001). This paleoclimatic shift to more humid conditions initiated during the late Berriasian is recognized at the western Tethyan scale, as revealed by the onset of kaolinite-rich assemblages in sediments (Fig. 22; Deconinck, 1993; Schnyder et al., 2009; Morales et al., 2013) or by spectral gamma rays (Schnyder et al., 2006; Grabowski et al., 2013).

We suggest that geodynamic and climate changes together played a key role in the demise of carbonate production in the Paris Basin. Indeed, from the earliest late Tithonian to the latest Berriasian, a cumulative uplift of the study area by ~120 m is calculated, which was even greater laterally to the north, closer to the London-Brabant Massif, and possibly to the south on the edge of the syncline created (Fig. 20). During the JCU, the climate was relatively drier and no karstification affected the Tithonian or underlying carbonates. Although, at the onset of the RU, the climate was still semi-arid, it became more humid during the sedimentary *hiatus* linked to this unconformity. As a consequence, weathering processes may have occurred and particularly affected the

limestone on the edges of the rejuvenated/emphasized syncline, forming kaolinite-rich soils or iron crust in soils (Fig. 21; Thiry et al., 2006; Fizaine, 2012). Iron-rich deposits, intensively exploited during the nineteenth century, have been extracted from karstic cavities perforating the *Calcaire du Barrois* within the Mélaire mines (Corroy, 1925; Fizaine, 2012). Iron ore consists of iron ooids and iron-rich sandstones (Thiry et al., 2006; Fizaine, 2012), as observed in the lower part of the *Sables de Griselles* Formation in the Terme quarry (Fig. 12F). A part of the iron products may be concentrated in the negative zones of the paleo-karstic relief, at the onset of the deposition of the *Sables de Griselles* during the latest Berriasian (Hilly and Haguenauer, 1979). Iron-rich sandstones attributed to the early Valanginian are also described close to Montiers-sur-Saulx (Fizaine, 2012), suggesting that ferruginous weathering products can be formed throughout the study area during the latest Berriasian and early Valanginian. Lateritic alteration may have occurred laterally to the study area, and particularly to the north toward the London-Brabant massif where thick kaolinite-rich soil could have formed during the early Cretaceous (Thiry et al., 2006). The onset of a kaolinite-rich clay assemblage in marine sediments at the late Berriasian over the western Tethyan domain (*e.g.* Schnyder et al., 2009) is compatible with the extensive development of kaolinite soils. Increasingly wet and cool conditions favored terrigenous influxes from the increasingly eroded exposed crystalline and sedimentary basement around the Paris Basin (Armorican and London-Brabant massifs;

Fig. 20. Structural scheme from the late Tithonian to early Valanginian in the eastern Paris Basin in four successive steps. A- Late Tithonian. B- Jurassic/Cretaceous boundary. C- Early Berriasian. D- Late Berriasian. E-Late Berriasian to early Valanginian.

Allen, 1959), and the deposition of the *Sables de Griselles*. Development of distributary channels in a delta plain environment possibly reinforced the irregular aspect of the RU-related surface, through a set of incisions, although it is not possible to estimate precisely the relative impact of karstification before the incision. More humid conditions from late Berriasian favor weathering and detrital inputs which were very unfavorable to carbonate production.

This was a critical period in the development of the basin since significant amounts of meteoric fluids penetrated down into the underlying Mid/Late Jurassic limestones exposed on the basin edges, where they were at the origin of extensive cementation stages dramatically reducing reservoir properties (Vincent et al., 2007; Brigaud et al., 2009; Carpentier et al., 2014; Blaise et al., 2015; Pisapia et al., 2017). This is also true deeper in the stratigraphy where meteoric fluids
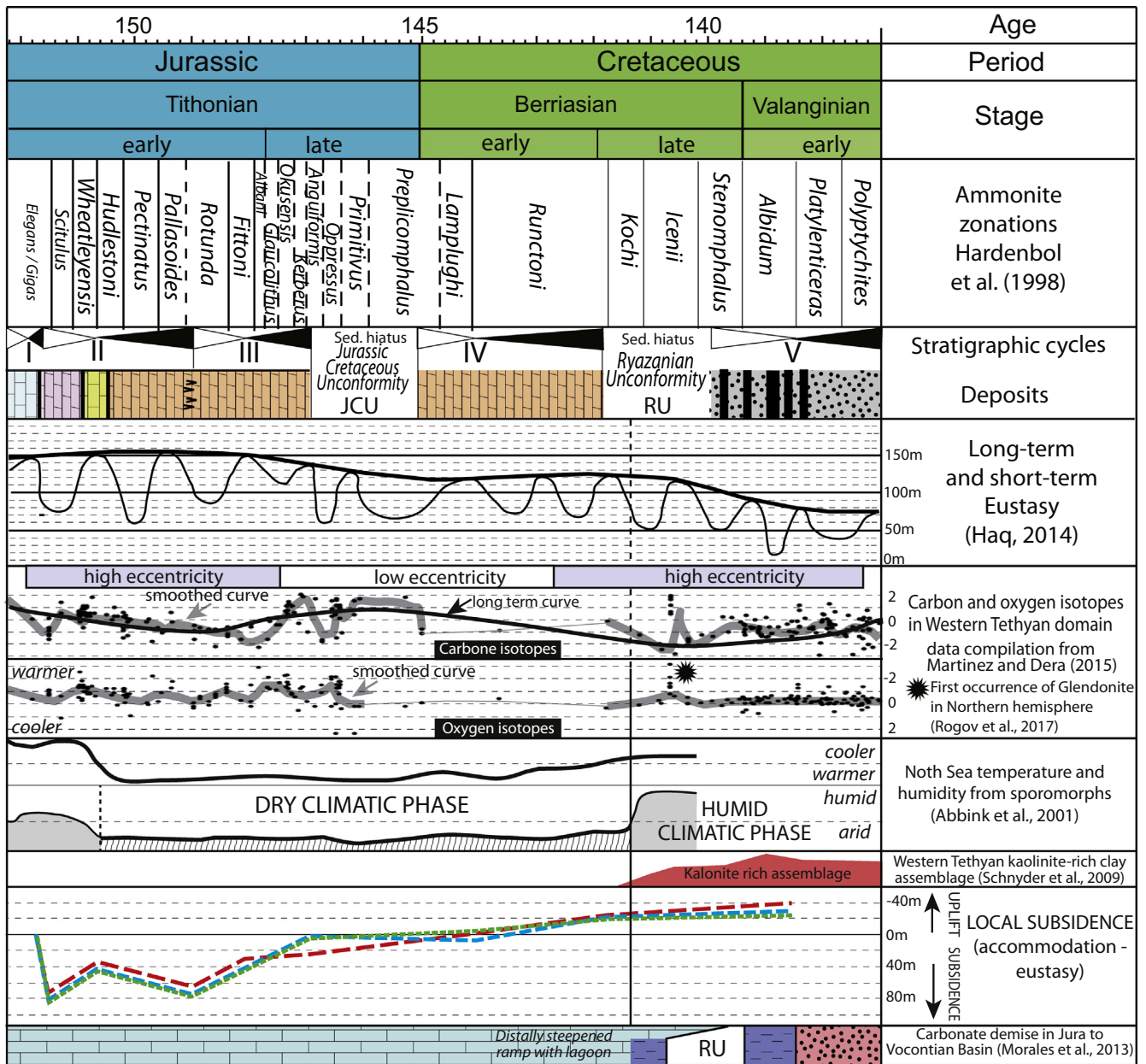
Fig. 21. Synthetic chronostratigraphic diagram from the Tithonian to Valanginian showing eastern Paris Basin sequences, sedimentary facies, long-term and short-term eustasy (Haq, 2014), low and high eccentricity periods (Martinez and Dera, 2015), δ¹³C and δ¹⁸O of belemnites in the western Tethyan domain (‰ V-PDB, grey curve: smoothed δ¹³C and δ¹⁸O, Martinez and Dera, 2015), North Sea temperature and humidity from sporomorphs (Abbink et al., 2001), calculated subsidence in the eastern Paris Basin and two depositional systems.

originated world-class fluorite deposits at the basement/sediment unconformity (Gigoux et al., 2015; Gigoux et al., 2016).

6. Conclusion

This study provides new insights into clearly exposed local responses of sedimentary change to large-scale climatic and geodynamic forcing factors. By integrating sedimentary facies analysis, carbonate diagenesis, isotopic geochemistry, and subsidence quantification carried out in the eastern part of the Paris Basin we have deciphered the respective influences of geodynamics and climate on critical changes at the Jurassic/Cretaceous boundary. Fourteen lithofacies were characterized in five sedimentary environments (1) storm-dominated upper offshore, (2) shoal, (3) lagoon, (4) supratidal, brackish to brine ponds and marshes, and (5) delta plain environment. A high-resolution sequence stratigraphy scheme was drawn up at the ammonite biozone scale, with the identification of five third-order depositional sequences

(Sequences I to V), that can be easily be integrated into existing stratigraphic schemes on the scale of western European basins.

Two distinct depositional environments were defined for the Tithonian to early Valanginian interval, (1) a classical carbonate ramp model, and (2) an upper deltaic plain model. Within the carbonate ramp, a facies change from limestones to dolomites ("Purbeckian" facies) occurred at the end of the early Tithonian. The establishment of dry and warm conditions, deduced from a compilation of sporomorph occurrences and oxygen isotopes on belemnites in the western Tethyan domain, clearly influenced the dolomitization process and prevented any meteoric diagenesis in surface aquifers. All macroscopic (stratiform aspect of dolomite bodies, anhydrite pseudomorphs, collapse breccias) and microscopic (fine crystalline replacive dolomite) evidence, as well as heavy δ¹⁸O values (+2‰ to +4‰) indicate an early sabkha dolomitization process.

A sedimentary gap within the "Purbeckian" facies is characterized during the late Tithonian and corresponds to the Jurassic–Cretaceous

Unconformity (JCU), which is well documented in European basins. This unconformity is an important structural episode in the Paris Basin marked by (1) an estimated accumulative uplift of 80 m during Sequence III and by (2) the formation of a local NW–SE low wavelength 15 km-wide and 30 km-long flexure in the study area. We suspect that NE–SW compression in the Paris Basin induced this flexure, as already observed in northern France (Guillocheau et al., 2000). This flexural event is interpreted as a consequence of the extensional tectonics in southern and northern Europe, related to the opening of the central and north Atlantic Ocean (Ziegler, 1988; Jacquin and de Graciansky, 1998a). After this important event recorded at the Jurassic/Cretaceous boundary, supratidal sedimentation resumed with new dolomitic facies. The major depositional change occurred between the early and late Berriasian, with a sharp contact between shallow carbonate platform facies and overlying fluviatile-deltaic clastic deposits (Wealden facies). This major sedimentary change corresponds to a second large sedimentary hiatus known as the Ryazanian unconformity (RU). This unconformity is associated with the development of karst in the study area and more broadly in the NE Paris Basin, with a cumulative uplift of 120 m, and the development of ferruginous weathering products (goethite). The rifting phase in the Bay of Biscay, in the Pyrenean Rift Zone, and the end of rifting in North Sea together with the opening of the Ligurian Sea, which is approximately 700 km south of the eastern Paris Basin, had a major influence on the northern part of France by causing uplifts along the eastern border of the Armorican Massif, the Poitou High, and the southern border of the London-Brabant Massif. The late Berriasian–early Valanginian was a high eccentricity period dominated by warm conditions, normally climatically favorable to carbonate platform development in the western Tethyan domain, but this period was marked by near-freezing conditions in the northern hemisphere and by humid conditions in the North Sea area. These climatic conditions may have locally favored terrigenous influx from terrestrial to marine domains in western European basins. Added to the generalized uplift, these local cooler and more humid conditions favoring detrital inputs were definitively unfavorable to carbonate growth, and were at the origin of the total demise of the carbonate platform in the Paris Basin.

Acknowledgments

References

Abbink, O., Targarona, J., Brinkhuis, H., Visscher, H., 2001. Late Jurassic to earliest Cretaceous palaeoclimatic evolution of the southern North Sea. Global and Planetary Change 30, 231–256.

Al-Aasm, I.S., Taylor, B., South, B., 1990. Stable isotope analysis of multiple carbonate samples using selective acid extraction. Chemical Geology 80, 119–125.

Allen, P., 1959. The Wealden environment: Anglo-Paris Basin. Philosophical Transactions of the Royal Society, B: Biological Sciences 242, 283–346.

Allen, P., 1998. Purbeck-Wealden (early Cretaceous) climates. Proceedings of the Geologists Association 109, 197–236.

Allen, A., Allen, J.R., 2005. Basin analysis: principles and applications. 2nd edition. Blackwell Publishing, Oxford, p. 549p.

Allen, P., Wimbledon, W.A., 1991. Correlation of NW European Purbeck-Wealden (nonmarine Lower Cretaceous) as seen from English type-areas. Cretaceous Research 12, 511–526.

Andrieu, S., Brigaud, B., Barbarand, J., Lasseur, E., Saucède, T., 2016. Disentangling the control of tectonics, eustasy, trophic conditions and climate on shallow-marine carbonate production during the Aalenian–Oxfordian interval: from the western France platform to the western Tethyan domain. Sedimentary Geology 345, 54–84.

Andrieu, S., Brigaud, B., Barbarand, J., Lasseur, E., 2018. The complex diagenetic history of discontinuities in shallow-marine carbonate rocks: new insights from high-resolution ion microprobe investigation of $\delta^{18}O$ and $\delta^{13}C$ of early cements. Sedimentology 65, 360–399.

Arbey, F., 1980. Les formes de la silice et l'identification des évaporites dans les formations silicifiées. Bulletin des Centres de Recherches Exploration-Production Elf-Aquitaine 4, 309–365.

Blaise, T., Barbarand, J., Kars, M., Ploquin, F., Aubourg, C., Brigaud, B., Cathelineau, M., El Albani, A., Gautheron, C., Izart, A., Janots, D., Michels, R., Pagel, M., Pozzi, J.-P., Boiron, M.-C., Landrein, P., 2014. Reconstruction of low temperature (<100 °C) burial in sedimentary basins: a comparison of geothermometer in the intracontinental Paris Basin. Marine and Petroleum Geology 53, 71–87.

Blaise, T., Tarantola, A., Cathelineau, M., Boulvais, P., Techer, I., Rigaudier, T., Boiron, M.-C., Pierron, O., Landrein, P., 2015. Evolution of porewater composition through time in limestone aquifers: salinity and D/H of fluid inclusion water in authigenic minerals (Jurassic of the eastern Paris Basin, France). Chemical Geology 417, 210–227.

Brigaud, B., Pucéat, E., Pellenard, P., Vincent, B., Joachimski, M.M., 2008. Climatic fluctuations and seasonality during the Late Jurassic (Oxfordian-Early Kimmeridgian) inferred from $\delta^{18}O$ of Paris Basin oyster shells. Earth and Planetary Science Letters 273, 58–67.

Brigaud, B., Durlet, C., Deconinck, J.-F., Vincent, B., Thierry, J., Trouiller, A., 2009. The origin and timing of multiphase cementation in carbonates: impact of regional scale geodynamic events on the Middle Jurassic Limestones diagenesis (Paris Basin, France). Sedimentary Geology 222, 161–180.

Brigaud, B., Vincent, B., Carpentier, C., Robin, C., Guillocheau, F., Yven, B., Huret, E., 2014. Growth and demise of the Jurassic carbonate platform in the intracratonic Paris Basin (France): interplay of climate change, eustasy and tectonics. Marine and Petroleum Geology 53, 3–29.

Buissart, H., Clement, M., Leblanc, M., 1988. Eléments nouveaux sur le faciès wealdien au Nord-Est de Paris. Annales. Société Géologique du Nord 107, 155–176.

Carpentier, C., Brigaud, B., Blaise, T., Vincent, B., Durlet, C., Boulvais, P., Pagel, M., Hibsch, C., Yven, B., Lach, P., Cathelineau, M., Boiron, M.-C., Landrein, P., Buschaert, S., 2014. Impact of basin burial and exhumation on Jurassic carbonates diagenesis on both sides of a thick clay barrier (Paris Basin, NE France). Marine and Petroleum Geology 53, 44–70.

Catuneanu, O., Galloway, W.E., Kendall, C.G.S.C., Miall, A.D., Posamentier, H.W., Strasser, A., Tucker, M.E., 2011. Sequence stratigraphy: methodology and nomenclature. Newsletters on Stratigraphy 44, 173–245.

Corroy, G., 1925. Le Néocomien de la bordure orientale du Bassin de Paris (Thèse de doctorat Thesis, Nancy, 335 pp.).

Cottençon, A., Parant, B., Flaceliere, G., 1975. Lower Cretaceous Gas-fields in Holland. Petroleum and the continental shelf of north-west Europe 1 pp. 402–412.

Deconinck, J.-F, 1987. Minéraux argileux des faciès purbeckiens: Jura suisse et français, Dorset (Angleterre) et Boulonnais (France). Annales. Société Géologique du Nord 56, 285–297.

Deconinck, J.-F., 1993. Clay mineralogy of the Late Tithonian-Berriasian deep-sea carbonates of the Vocontian Trough (SE France): relationships with sequence stratigraphy. Bulletin des Centres de Recherches Exploration-Production Elf-Aquitaine 17, 223–234.

Deconinck, J.-F., Strasser, A., 1987. Sedimentology, clay mineralogy and depositional environment of Purbeckian green marls (Swiss and French Jura). Eclogae Geologicae Helvetiae 80, 753–772.

Deconinck, J.-F., Strasser, A., Debrarant, P., 1988. Formation of illitic minerals at surface temperatures in Purbeckian sediments (Lower Berriasian, Swiss and French Jura). Clay Minerals 23, 91–103.

Deconinck, J.-F., Baudin, F., Tribovillard, N., 2000. The Purbeckian facies of the Boulonnais: a tsunami deposit hypothesis (Jurassic–Cretaceous boundary, northern France). Comptes Rendus de l'Académie des Sciences - Series IIA - Earth and Planetary Science 330, 527–532.

Deconinck, J.-F., Gillot, P.Y., Steinberg, M., Strasser, A., 2001. Syn-depositional, low temperature illite formation at the Jurassic-Cretaceous boundary (Purbeckian) in the Jura Mountains (Switzerland and France); K/Ar and delta 18 O evidence. Bulletin de la Société Géologique de France 172, 343.

Dera, G., Brigaud, B., Monna, F., Laffont, R., Puceat, E., Deconinck, J.F., Pellenard, P., Joachimski, M.M., Durlet, C., 2011. Climatic ups and downs in a disturbed Jurassic world. Geology 39, 215–218.

Dercourt, J., Gaetani, M., Vrielynck, B., Barrier, E., Biju Duval, B., Brunet, M., Cadet, J., Crasquin, S., Sandulescu, M., 2000. Atlas Peri-Tethys, Palaeogeographical Maps, 24 Maps and Explanatory Notes: I–XX. CCGM/CGMW, Paris, pp. 1–269.

Doré, A., Lundin, E., Jensen, L., Birkeland, Ø., Eliassen, P., Fichler, C., 1999. Principal tectonic events in the evolution of the northwest European Atlantic margin. Geological Society, London, Petroleum Geology Conference series 5, 41–61.

Durlet, C., Loreau, J.P., 1996. Inherent diagenetic sequence of hardgrounds resulting from marine ablation of exposure surfaces. Example of the Burgundy platform, Bajocian (France). Comptes Rendus de l'Academie des Sciences Serie II Fascicule A- Sciences de la Terre et des Planetes 323, 389–396.

Durlet, C., Loreau, J.P., Pascal, A., 1992. Diagenetic signature of unconformities and new graphic visualization of diagenesis. Comptes Rendus de l' Academie des Sciences Serie IIa: Sciences de la Terre et des Planets 314, 1507–1514.

Enay, R., Mangold, C., 1980. Synthèse paléogéographique du Jurassique français. Document du Laboratoire de Géologie de Lyon Volume 5. Groupe Français d'Etude du Jurassique (220 pp.).

Fizaine, J.-P., 2012. Les paléokarsts et les formations ferrugineuses associées dans le Bassin parisien et ses bordures: caractérisation et évolutions géomorphologiques. Université de Lorraine, Nancy (468 pp.).

Gigoux, M., Delpech, G., Guerrot, C., Pagel, M., Augé, T., Négrel, P., Brigaud, B., 2015. Evidence for an Early Cretaceous mineralizing event above the basement/sediment unconformity in the intracratonic Paris Basin: paragenetic sequence and Sm-Nd dating of the world-class Pierre-Perthuis stratabound fluorite deposit. Mineralium Deposita 50, 455–463.

Gigoux, M., Brigaud, B., Pagel, M., Delpech, G., Guerrot, C., Augé, T., Négrel, P., 2016. Genetic constraints on world-class carbonate- and siliciclastic-hosted stratabound fluorite deposits in Burgundy (France) inferred from mineral paragenetic sequence and fluid inclusion studies. Ore Geology Reviews 72, 940–962.

Grabowski, J., Schnyder, J., Sobień, K., Koptíková, L., Krzemiński, L., Pszczółkowski, A., Hejnar, J., Schnabl, P., 2013. Magnetic susceptibility and spectral gamma logs in the Tithonian–Berriasian pelagic carbonates in the Tatra Mts (Western Carpathians, Poland): palaeoenvironmental changes at the Jurassic/Cretaceous boundary. Cretaceous Research 43, 1–17.

Gradstein, F.M., Ogg, J.G., Schmitz, M., Ogg, G., 2012. The Geologic Time Scale 2012. Elsevier BV (1144 pp.).

Guillocheau, F., 1991. Large-scale transgressive-regressive cycles of tectonic origin into the Mesozoic sediments of the Paris Basin. Comptes Rendus de l'Academie des Sciences Serie II Fascicule A- Sciences de la Terre et des Planetes 312, 1587–1593.

Guillocheau, F., Robin, C., Allemand, P., Bourquin, S., Brault, N., Dromart, G., Friedenberg, R., Garcia, J.-P., Gaulier, J.-M., Gaumet, F., Grosdoy, B., Hanot, F., le Strat, P., Mettraux, M., Nalpas, T., Prija, C., Rigollet, C., Serrano, O., Grandjean, G., 2000. Meso-Cenozoic geodynamic evolution of the Paris Basin: 3D stratigraphic constraints. Geodinamica Acta 13, 189–245.

Haq, B.U., 2014. Cretaceous eustasy revisited. Global and Planetary Change 113, 44–58.

Haq, B.U., 2018. Jurassic sea-level variations: a reappraisal. GSA Today 28, 4–10.

Hardenbol, J., Thierry, J., Farley, M.B., Jacquin, T., de Graciansky, P.-C., Vail, P.R., 1998. Mesozoic and Cenozoic sequence chronostratigraphic framework of European basins. In: De Graciansky, P.-C., Hardenbol, J., Jacquin, T., Vail, P.-R. (Eds.), Mesozoic and Cenozoic sequence stratigraphy of European basins. SEPM Special Publication 60, pp. 3–13.

Hendry, J.P., 1993. Geological control on regional subsurface carbonate cementation: an isotopic paleohydrologic investigation of middle Jurassic limestones in Central England. In: Horbury, A.D., Robinson, A.G. (Eds.), Diagenesis and Basin Development. AAPG Studies in Geology. AAPG 36, pp. 231–260.

Hesselbo, S.P., Allen, P., 1991. Major erosion surfaces in the basal Wealden Beds, Lower Cretaceous, south Dorset. Journal of the Geological Society, London 148, 105–113.

Hillgärtner, H., Strasser, A., 2003. Quantification of high-frequency sea-level fluctuations in shallow-water carbonates: an example from the Berriasian–Valanginian (French Jura). Palaeogeography, Palaeoclimatology, Palaeoecology 200, 43–63.

Hilly, J., Haguenauer, B., 1979. Lorraine-Champagne, Guides géologiques régionaux. Masson, Paris.

Homberg, C., Schnyder, J., Benzaggagh, M., 2013. Late Jurassic-Early Cretaceous faulting in the Southeastern French Basin: does it reflect a tectonic reorganization? Bulletin de la Société Géologique de France 184, 501–514.

Jacquin, T., de Graciansky, P.-C., 1998a. Major transgressive/regressive cycles: the stratigraphic signature of European basin development. In: De Graciansky, P.-C., Hardenbol, J., Jacquin, T., Vail, P.-R. (Eds.), Mesozoic and Cenozoic Sequence Stratigraphy of European Basins. SEPM Special Publication 60, pp. 15–29.

Jacquin, T., de Graciansky, P.-C., 1998b. Transgressive/regressive (second order) facies cycles: the effects of tectono-eustasy. In: De Graciansky, P.-C., Hardenbol, J., Jacquin, T., Vail, P.-R. (Eds.), Mesozoic and Cenozoic Sequence Stratigraphy of European Basins. SEPM Special Publication 60, pp. 31–42.

Jacquin, T., Dardeau, G., Durlet, C., de Graciansky, C., Hantzpergue, P., 1998a. The North Sea Cycle: an overview of 2nd-order transgressive/regressive facies cycles in western Europe. In: de Graciansky, P.-C., Hardenbol, J., Jacquin, T., Vail, P.R. (Eds.), Mesozoic and Cenozoic Sequence Stratigraphy of European Basins. SEPM Special Publication 60, pp. 445–466.

Jacquin, T., Rusciadelli, G., Amedro, F., de graciansky, P.-C., Magniez-jannin, F., 1998b. The North Atlantic cycle: an overview of 2nd-order transgressive/regressive facies cycles in the Lower Cretaceous of Western Europe. In: de Graciansky, P.-C., Hardenbol, J., Jacquin, T., Vail, P.R. (Eds.), Mesozoic and Cenozoic Sequence Stratigraphy of European Basins. SEPM Special Publication 60, pp. 397–409.

Joachimski, M.M., 1994. Subaerial exposure and deposition of shallowing upward sequences - evidence from stable isotopes of Purbeckian peritidal carbonates (basal Cretaceous, Swiss and French Jura mountains. Sedimentology 41, 805–824.

KyrkjebØ, R., Gabrielsen, R.H., Faleide, J.I., 2004. Unconformities related to the Jurassic-Cretaceous synrift-post-rift transition of the northern North Sea. Journal of the Geological Society 161, 1–17.

Lake, S.D., Karner, G.D., 1987. The structure and evolution of the Wessex Basin, southern England - an example of inversion tectonics. Tectonophysics 137, 347–378.

Lorenz, H., Lehrberger, G., 2013. Savonnières, Morley & Co.: Oolithische Kalksteine aus Lothringen (Frankreich) als Bau-und Denkmalgesteine in Mitteleuropa. Tagung für Ingenieurgeologie mit Forum für junge Ingenieurgeologen. 19, 359–365.

Martinez, M., Dera, G., 2015. Orbital pacing of carbon fluxes by a approximately 9-My eccentricity cycle during the Mesozoic. Proceedings of the National Academy of Sciences 112, 12604–12609.

Mégnien, C., Mégnien, F., 1980. Synthèse géologique du Bassin de Paris. Memoire du BRGM 101 (446 pp.).

Meyer, R., 1976. Continental sedimentation, soil genesis,and marine transgression in the basal beds of the Cretaceous in the east of the Paris Basin. Sedimentology 23, 235–253.

Miller, K.G., Kominz, M.A., Browning, J.V., Wright, J.D., Mountain, G.S., Katz, M.E., Sugarman, P.J., Cramer, B.S., Christie-Blick, N., Pekar, S.F., 2005. The Phanerozoic record of global sea-level change. Science 310, 1293–1298.

Montadert, L., Roberts, D.G., De Charpal, O., Guennoc, P., 1979. Rifting and subsidence of the northern continental margin of the Bay of Biscay. Initial Reports of the Deep Sea Drilling Project. U.S. Government Printing Office, Washington (1025–1060 pp.).

Morales, C., Gardin, S., Schnyder, J., Spangenberg, J., Arnaud-Vanneau, A., Arnaud, H., Adatte, T., Föllmi, K.B., Weissert, H., 2013. Berriasian and early Valanginian environmental change along a transect from the Jura Platform to the Vocontian Basin. Sedimentology 60, 36–63.

Mosar, J., Eide, E.A., Osmundsen, P.T., Sommaruga, A., Torsvik, T.H., 2002. Greenland – Norway separation: a geodynamic model for the North Atlantic. Journal of Geology 82, 282–299.

Oakman, C., Partington, M., 1998. Cretaceous. Petroleum Geology of the North Sea: Basic Concepts and Recent Advances, Fourth Edition, pp. 294–349.

Pagel, M., Barbarand, J., Beaufort, D., Gautheron, C., Pironon, J., 2014. Bassins sédimentaires-les marqueurs de leur histoire thermique. EDP Sciences (225 pp.).

Pharaoh, T., Dusar, M., Geluk, M., Kockel, F., Krawczyk, C., Krzywiec, P., Scheck-Wenderoth, M., Thybo, H., Vejbaek, O., van Wees, J.D., 2010. Tectonic evolution. Petroleum Geological Atlas of the Southern Permian Basin Area. EAGE, Houten, The Netherlands, pp. 24–57.

Pisapia, C., Deschamps, P., Battani, A., Buschaert, S., Guihou, A., Hamelin, B., Brulhet, J., 2017. U/Pb dating of geodic calcite: new insights on Western Europe major tectonic events and associated diagenetic fluids. Journal of the Geological Society 175, 60–70.

Plint, A.G., 2010. In: James, N.P., Dalrymple, R.W. (Eds.), Wave- and Storm-dominated Shoreline and Shallow-marine Systems. Facies Models 4. Geological Association of Canada, St. John's, Newfoundland, pp. 167–199.

Pomar, L., 2001. Types of carbonate platforms: a genetic approach. Basin Research 13, 313–334.

Pomar, L., Baceta, J.I., Hallock, P., Mateu-Vicens, G., Basso, D., 2017. Reef building and carbonate production modes in the west-central Tethys during the Cenozoic. Marine and Petroleum Geology 83, 261–304.

Ramail, N., 2005. Carbonate Sedimentology, Sequence Stratigraphy, and Cyclostratigraphy of the Tithonian in the Swiss and French Jura Mountains. Université de Fribourg, Fribourg (246 pp.).

Rawson, P.F., Riley, L.A., 1982. Latest Jurassic-Early Cretaceous events and the "late Cimmerian unconformity" in North Sea area. American Association of Petroleum Geologists Bulletin 66, 2628–2648.

Riboulleau, A., Baudin, F., Daux, V., Hantzpergue, P., Renard, M., Zakharov, V., 1998. Evolution de la paléotempérature des eaux de la plate-forme russe au cours du Jurassique supérieur. Comptes Rendus de l'Académie des Sciences 326, 239–246.

Robin, C., Guillocheau, F., Allemand, P., Bourquin, S., Dromart, G., Gaulier, J.M., Prijac, C., 2000. Time and space-scales of the tectonic control of a flexural intracratonic basin: the Paris Basin. Bulletin de la Société Géologique de France 171, 181–196.

Rogov, M.A., Ershova, V.B., Shchepetova, E.V., Zakharov, V.A., Pokrovsky, B.G., Khudoley, A.K., 2017. Earliest Cretaceous (late Berriasian) glendonites from Northeast Siberia revise the timing of initiation of transient Early Cretaceous cooling in the high latitudes. Cretaceous Research 71, 102–112.

Rowley, D.B., 2013. Sea level: earth's dominant elevation—implications for duration and magnitudes of sea level variations. The Journal of Geology 121, 445–454.

Ruffell, A.H., Rawson, P.F., 1994. Palaeoclimate control on sequence stratigraphic patterns in the late Jurassic to mid-Cretaceous, with a case study from Eastern England. Palaeogeography, Palaeoclimatology, Palaeoecology 110, 43–54.

Rusciadelli, G., 1996. Stratigraphie séquentielle et modélisation de l'espace disponible du Jurassique supérieur et du Crétacé inférieur du Bassin de Paris. Université Paris-Sud, Orsay (200 pp.).

Sahagian, D., Pinous, O., Olferiev, A., Zakharov, V., 1996. Eustatic curve for the Middle Jurassic–Cretaceous based on Russian platform and Siberian stratigraphy: zonal resolution. American Association of Petroleum Geologists Bulletin 80, 1433–1458.

Schlager, W., 2004. Fractal nature of stratigraphic sequences. Geology 32, 185–188.

Schnyder, J., Baudin, F., Deconinck, J.-F., 2005a. A possible tsunami deposit around the Jurassic–Cretaceous boundary in the Boulonnais area (northern France). Sedimentary Geology 177, 209–227.

Schnyder, J., Gorin, G., Soussi, M., Baudin, F., Deconinck, J.-F., 2005b. Enregistrement de la variation climatique au passage Jurassique/Crétacé sur la marge sud de la Téthys: minéralogie des argiles et palynofaciès de la coupe du Jebel Meloussi (Tunisie centrale, formation Sidi Kralif). Bulletin de la Société Géologique de France 176, 171–182.

Schnyder, J., Ruffell, A., Deconinck, J.-F., Baudin, F., 2006. Conjunctive use of spectral gamma-ray logs and clay mineralogy in defining late Jurassic–early Cretaceous palaeoclimate change (Dorset, UK). Palaeogeography, Palaeoclimatology, Palaeoecology 229, 303–320.

Schnyder, J., Baudin, F., Deconinck, J.-F., 2009. Occurrence of organic-matter-rich beds in Early Cretaceous coastal evaporitic setting (Dorset, UK): a link to long-term palaeoclimate changes? Cretaceous Research 30, 356–366.

Sellwood, B.W., Shepherd, T.J., Evans, M.R., James, B., 1989. Origin of late cements in oolitic reservoir facies: a fluid inclusion and isotopic study (Mid-Jurassic, southern England). Sedimentary Geology 61, 223–237.

Simone, L., Bravi, S., Carannante, G., Masucci, I., Pomoni-Papaioannou, F., 2012. Arid versus wet climatic evidence in the "middle Cretaceous" calcareous successions of the Southern Apennines (Italy). Cretaceous Research 36, 6–23.

Steckler, M.S., Watts, A.B., 1978. Subsidence of the Atlantic-type continental margin off New-York. Earth and Planetary Science Letters 41, 1–13.

Stoker, M.S., Stewart, M.A., Shannon, P.M., Bjerager, M., Nielsen, T., Blischke, A., Hjelstuen, B.O., Gaina, C., McDermott, K., Ólavsdóttir, J., 2016. An overview of the Upper Palaeozoic–Mesozoic stratigraphy of the NE Atlantic region. In: Péron-Pinvidic, G., Hopper, J.R., Stoker, M.S., Gaina, C., Doornenbal, J.C., Funck, T., Arting, U.E. (Eds.), The NE Atlantic Region: A Reappraisal of Crustal Structure, Tectonostratigraphy and Magmatic Evolution. Geological Society, London, Special Publications 447, pp. 11–68.

Strasser, A., 1988. Shallowing-upward sequences in Purbeckian peritidal carbonates (lowermost Cretaceous, Swiss and French Jura Mountains). Sedimentology 35, 369–383.

Strauss, C., Eltsner, F., Jan du Chene, R., Mutterlose, J., Reiser, H., Brandt, K.-H., 1993. Micro-paleontological evidence and palynological evidence on the stratigraphical position of the "German Wealden" in NW-Germany. Zitteliana 20, 389–401.

Surlyk, F., 2003. The Jurassic of East Greenland: a sedimentary record of thermal subsidence, onset and culmination of rifting. Geological Survey of Denmark and Greenland Bulletin 1, 659–722.

Thierry, J., Barrier, E., 2000. Early Tithonian - map 11. In: Dercourt, J., Gaetani, M., Vrielynck, B., Barrier, E., Biju Duval, B., Brunet, M.F., Cadet, J.P., Crasquin, S., Sandulescu, M. (Eds.), Atlas Peri-Tethys, Palaeogeographical Maps. CCGM/CGMW, Paris.

Thiry, M., Quesnel, F., Yans, J., Wyns, R., Anne, V., Théveniaut, H., Simon-Coincon, R., Ricordel, C., Moreau, M.G., Giot, D., Dupuis, C., Bruxelles, L., Barbarand, J., Baele, J.M., 2006. Continental France and Belgium during the early Cretaceous: paleoweatherings and paleolandforms. Bulletin de la Société Géologique de France 177, 155–175.

Underhill, J.R., Partington, M.A., 1993. Jurassic thermal doming and deflation in the North Sea: implications of the sequence stratigraphic evidence. Geological Society, London, Petroleum Geology Conference series 4, 337–345.

Vincent, B., Emmanuel, L., Houel, P., Loreau, J.-P., 2007. Geodynamic control on carbonate diagenesis: petrographic and isotopic investigation of the Upper Jurassic formations of the Paris Basin (France). Sedimentary Geology 197, 267–289.

Warren, J., 2000. Dolomite: occurrence, evolution and economically important associations. Earth-Science Reviews 52, 1–81.

Ziegler, P.A., 1988. Evolution of the Artic-North Atlantic and the western Tethys - a visual presentation of a series of paleogeographic paleotectonic maps. Memoir - American Association of Petroleum Geologists 43 (164–196 pp.).

Ziegler, P.A., 1990. Geological Atlas of Western and Central Europe. Publication 148. Elsevier, Geological Society, Shell Internationale Petroleum Maatschappij, Amsterdam (256 pp.).

Ziegler, P.A., 1992. North Sea rift system. Tectonophysics 208, 55–75.